Classification, segmentation and correlation of zoned minerals

Tom Sheldrake[1*]; Oliver Higgins[1]**

[1]Department of Earth Sciences, University of Geneva, Rue des Maraîchers 13, 1205 Genève
*corresponding author (thomas.sheldrake@unige.ch) twitter: @NatHazTom
**co-author (oliver.higgins@unige.ch)

THIS IS A NON-PEER REVIEW PREPRINT SUBMITTED TO COMPUTERS AND GEOSCIENCES

Authorship statement: TS designed and wrote the code. TS and OH tested the code and wrote the manuscript.

Highlights:

- New methodology to classify minerals in a thin section, using a finite-mixture model approach.
- Using image processing techniques, chemical zonation within phenocrysts has been segmented and correlated across multiple thin sections
- The approach has been used to classify minerals in thin sections of volcanic rocks, and the to correlate zonation within plagioclase phenocrysts.

Computer code availability

. Name of code: Mineral zonation CSC (Classification, Segmentation and Correlation)
. Developers : Tom Sheldrake
. Contact details : Departments of Earth Sciences, University of Geneva, Rue des Maraîchers 13, Genève 1205, Suisse; e-mail: thomas.sheldrake@unige.ch
. Year first available : 2021
. Hardware required : Mineral zonation CSC was run on a computer with 4 cores (4.0 GHz each) and 16 GB RAM.
. Software required: Mineral zonation CSC was run using RStudio and requires the following packages – *flexmix*, *dplyr*, *plyr*, *raster*, *pheatmap*, *pracma*, *pbapply*, *conicfit*, *viridis*, *imager*, and *apcluster*.
. Program language : the code is written in R v4.0
. Program size : 171.1 Mb
. Details on how to access the source code: the source files of *Mineral zonation CSC* can be downloaded from github : https://github.com/tom-sheldrake/Mineral-zonation-CSC

. Name of code: Mineral Classification
. Developers : Tom Sheldrake
. Contact details: Departments of Earth Sciences, University of Geneva, Rue des Maraîchers 13, Genève 1205, Suisse; e-mail: thomas.sheldrake@unige.ch
. Year first available : 2021
. Hardware required : Mineral Classification was run on a computer with 4 cores (4.0 GHz each) and 16 GB RAM.
. Software required: Mineral Classification was run using RStudio and requires the following packages – *flexmix*, *dplyr*, *plyr*, and *raster*.
. Program language : the code is written in R v4.0
. Program size : 44.3 Mb
. Details on how to access the source code : the source files of *Mineral classification* can be downloaded from github : https://github.com/tom-sheldrake/Mineral-Classification.

Abstract:

Minerals exhibit zoning patterns that can be related to changes in the environment in which they grew. Using statistical methods that have been designed to segment optical images, we have developed a procedure to segment zonation within minerals and correlate these zones between multiple crystals using elemental maps. This allows us to quantify the complexity and variability of chemical zoning between different geological samples. Specifically, we employ a simple linear iterative clustering algorithm, which splits the chemical maps into spatially constrained regions of similar chemistry. The result is a texturally segmented crystal, akin to what would be identified by the human eye. To aid the segmentation and correlation of zones, we also introduce a new method to classify multiple mineral phases within a single thin section. This is based on a finite mixture model approach, which proves very effective in removing mixed pixels that will only introduce noise into the segmentation. We provide an example using the mineral phase plagioclase. Using two contemporaneous samples from an eruptive unit on the island of St. Kitts we show that a volcanic bomb (~10cm) and scoria (~2cm) have similar rim compositions but distinctly different core compositions. Our methodology will enable a statistical characterization of 2D complexity of crystals in a variety of different geo-scientific disciplines. This will allow the genesis of different mineral phases to be characterised and directly compared.

Keywords: geochemistry, SLIC algorithm, Affinity Propagation, magma, volcano, plagioclase, anorthite

1. Introduction

Mineral composition is intrinsically linked to the environment in which it precipitated. Hence, when a mineral phase experiences different physical and chemical conditions during its growth, this manifests as chemical zoning. Chemical zoning in individual crystals can be imaged using electron spectroscopy by measuring, for example, variability in atomic density (e.g., backscatter electron; Ginibre et al., 2002) or luminescence (e.g., cathodoluminescence – CL; Hanchar & Miller, 1993; Watt et al., 1997; Lee et al., 2005). Changes in chemical composition can be related to micro-scale variability (e.g., boundary effects; Singer et al., 1995) or macro-scale variability due to changes in the larger state of the geological system (e.g., variation in intensive parameters; Ginibre et al., 2007). Hence, identifying and quantifying chemical zonation is an important tool to understand both micro- and macro-scale geological processes.

By visually inspecting crystal zoning throughout a geological sample, individual crystals can be targeted for quantitative analysis to help interpret the causal processes and their associated timescales. Measurements are commonly performed using transects from rim to core of a crystal, spanning the temporal history of its growth. Transects can be compared between crystals (Wallace & Bergantz, 2002), but this can be complicated by stretching of rim to core profiles due to sample cut effects (Cheng et al., 2017; Probst et al., 2018). Quantified crystals can be used as exemplars for groups of subjectively similar crystals, which is informed by the relative pattern of growth and the number of chemical zones present. Additionally, for particular mineral phases it can be possible to quantitatively calibrate BSE or CL images (e.g., Ginibre et al., 2002), providing the analytical conditions remain consistent and stable, and thus compare 2D variation within a thin section (Humphreys et al., 2013; Cheng et al., 2017).

Geochemical maps offer an opportunity to quantitatively compare crystal populations. However, no systematic approach exists to quantitatively correlate zoned crystals, resulting in uncertainty in the variability and statistical significance of different zoning patterns. The aim of the methodology presented here, is to resolve this issue by developing a semi-autonomous routine to analyse chemical maps and correlate crystal zonation. Our approach is designed around principles used in image segmentation and the concept of superpixels, which are defined as spatially constrained regions of pixels that have a similar composition (Achanta et al., 2012; Zhou, 2015). This approach is suited to mineral phases, which grow radially and so exhibit spatially constrained chemical zoning. Groups of superpixels are clustered together based on their average composition, such that

the zoning patterns do not necessarily replicate the pixel scale variability in chemical composition. The summary of 2D zonation is simplified in comparison to other methods that directly cluster the raw pixel data, and is thus more akin to the textural average that would be subjectively identified by eye (e.g., table 1 in Viccaro et al, 2010).

Our approach allows more robust quantitative comparison of the pattern and variability crystal zonation. For the correlation of segmented zones to be reliable, it is important that noisy data are removed a priori. One example of noisy data are so-called 'mixed pixels', which could be pixels that cross the boundary of two different mineral phases, or could be within a single crystal that contains cracks or smaller mineral or melt inclusions. Computational mineral grain separation is a well-established field, with many different approaches employed, including database querying (Gottlieb et al., 2000), multivariate regression (Willis et al., 2017), multivariate clustering (Wilson & MacRae, 2005; Lanari et al., 2014), and image segmentation methods using as superpixels (Maitre et al., 2019). However, the issue of mixed pixels is commonly approached in post-processing of the results (Lanari et al., 2019; Maitre et al., 2019), rather than integrated within the mineral separation algorithm. Instead, we have designed a new approach that accurately separates components of a thin section, of which mixed pixels represent one component. This approach is computationally slower (i.e. minutes vs seconds) than more traditional methods, but the results are more accurate with a focus on removing noisy pixels.

Magmatic minerals crystallised in igneous systems commonly exhibit zoning patterns that are related to changes in the state of the host magma (Bachmann & Dungan, 2002; Zellmer et al., 2003; Costa & Chakraborty, 2004; Humphreys et al., 2006; Pietranik et al., 2006; Ginibre et al., 2007; Shcherbakov et al., 2011; Druit et al., 2012; Cashman & Blundy, 2013; Ubide et al., 2015; Bennett et al., 2019; Cao et al., 2019; Weber et al., 2019; Higgins et al., 2021). This is particularly the case in volcanic samples, which can experience multiple different magmatic states during their dynamic journey to the surface. Interpreting these zoning patterns provides an insight into the magmatic processes that occur prior to an eruption. We present our method using thin sections of two volcanic samples collected from the island of St. Kitts in the Eastern Caribbean (**Fig. 1a**). We analyse two contemporaneous samples that represent the same volcanic unit, formed during an explosive basaltic eruption. However, one is a volcanic bomb with a long axis length of ~10cm (SK394C; **Fig. 1c**), whereas the other is a smaller scoriaceous deposit with a long axis of ~2cm (SK394A; **Fig. 1b**). Plagioclase and orthopyroxene phenocrysts are present in both samples, with oxide phases commonly in contact with the orthopyroxene. Amphibole phenocrysts are also

present in SK394A. Vesicularity exists in both samples, although vesicles are much larger in the volcanic bomb (SK394C) in comparison to the scoria (SK394A).

For each sample we prepared a thin section and measured a 1cm x 1cm map at a resolution of 20μm using a five-channel WDS detector in a JEOL JXA-8530F Electron Microprobe at the University of Lausanne. The operating conditions were as follows: an accelerating voltage of 15 keV, a beam current of 15 nA, a dwell time of 150 ms, and a beam diameter of 5μm. Our analyses focused on the mineral plagioclase, which exhibits distinct zoning in both samples. Quantitative analyses were made using transects in individual plagioclase crystals in SK394A, whose chemistry spanned the full variability observed. The operating conditions were as follows: an accelerating voltage of 15 keV, a beam current of 15 nA, a dwell time of 150 ms, and a beam diameter of 5μm. A variety of standards were used to quantify the major chemical components of plagioclase (orthoclase [Si^{4+}, K^{+}], andalusite [Al^{3+}], albite [Na^{+}], and wollastonite [Ca^{2+}]). In both samples the chemical variability of the plagioclase is dominantly controlled by the relative composition of the Ca^{2+} (anorthite) and Na^{+} (albite) end members (**Supplementary Fig. 1**). Consequently, in our analysis we use the counts of these two elements to segment and cluster textural features.

2. Proposed method

The methodology outlined in this manuscript has been developed to segment individual crystals and correlate zonation across many crystals in multiple thin-sections. Our approach is based on the following three fundamental steps:

1) Classification of the phenocrysts that are to be studied;
2) Segmentation of textural [spatial-chemical] zones in individual crystals;
3) Correlation of all segmented zones using a geochemical distance metric.

The data required for the first two steps is the raw intensity (integer counts) for the chemical elements of interest. For example, elemental maps of intensity can be measured by wavelength-dispersive spectroscopy (WDS) or energy-dispersive X-ray spectrometry (EDS) using an Electron microprobe (EMPA) or a Scanning Electron Microscope (SEM). Alternatively, a measure of intensity that varies systematically with specific chemical elements could be used (e.g. backscatter electrons and anorthite in plagioclase; Ginibre et al., 2002). For the third step, if the analytical conditions do

not vary between samples the measure of intensity can be directly compared. However, when samples are not mapped using identical analytical conditions, this step will require quantitative standardisation (e.g., converting intensity to wt. %) using a calibration curve for each sample, for the chemical elements of interest. This ensures different samples are directly comparable and enables quality assurance to be performed on the results. Alternatively, if a complete phase map has been already calibrated for each sample (e.g., XMapTools; Lanari et al., 2014, 2019), this could be used to segment and correlate zonation.

2.1 Classification

We first classify the different mineral phases that are present in the sample, using a two-dimensional finite Gaussian mixture model. This approach has the advantage that it excels at identifying mixed pixels (see discussion). It is based on the principle that for different minerals, elements that are present as network-modifying cations (e.g., Ca^{2+}, Mg^{2+}, K^{+}) occur in different proportions with respect to elements that are present as network-forming cations (e.g., Si^{4+}, Al^{3+}). Hence, by transforming the raw data according to the following two equations (**Eq. 1-2**), we end up with a series of two-dimensional Gaussian distributions that characterises each of the mineral phases present. Depending on the combination network-modifying cations (NMC) and network-forming cations (NFC) that are chosen, the E-M algorithm will separate mineral phases into different latent classes (i.e. clusters). To classify the chemical data into a series of latent classes we use the *Flexmix* package in R (Leisch, 2004), which uses an expectation-maximisation algorithm to implement the discrete mixture model.

$$X = 2 \cdot NFC + 1 \cdot NMC \quad \textbf{(1)}$$

$$Y = 1 \cdot NFC + 2 \cdot NMC \quad \textbf{(2)}$$

Multiple minerals may belong to the same latent class. This may happen because two phases have similar amounts of both the NMC and NFC (e.g., Al and Ca in orthopyroxene and oxides in **Fig. 2a-c**). Alternatively, if two minerals share similar covariance matrices (i.e. two elements vary in similar proportions in multiple minerals) they may also be allocated to the same latent class (e.g., amphibole and plagioclase in **Fig. 2a-c**). In this case, the two minerals are allocated to the same latent class because the EM algorithm has converged to a local maximum. If the EM algorithm had converged to the global maximum it would separate amphibole and plagioclase in **Fig. 2b**. The density of points belonging to these two phases is clearly distinguishable. However, because the

204 samples contain mostly matrix (**Fig. 1b-c**), the majority of pixels contain multiple mineral phases
205 and so convergence to a global maximum is difficult.
206
207 To overcome the issues of multiple phases belonging to the same latent class, we run the EM
208 algorithm for different combinations of NMC and NFC. The choice of elements should be informed
209 by an understanding of the sample that is being analysed (e.g., predominance of mafic vs. felsic
210 phases). For each combination of elements we search for the same number of latent class
211 components, although the EM algorithm may converge to a smaller (and thus different) number of
212 clusters. The number of latent class components is informed by optical microscopy and analysis of
213 the elemental maps and should be equal to or larger than the number of individual mineral phases
214 that can be observed (including matrix and vesicles/epoxy).
215
216 By running the EM algorithm for different combinations of NMC and NFC, we overcome the
217 problem of local convergence. For example, whilst Al-Ca cannot distinguish between orthopyroxene
218 and oxides (**Fig. 2a-c**), because Si is found in orthopyroxene but not oxides, Si-Ca does distinguish
219 these two phases (**Fig. 2d-f**). Furthermore, whilst Al-Ca cannot distinguish between plagioclase and
220 amphibole (**Fig. 2a-c**), it is possible with Si-Ca (**Fig. 2d-f**). This is because in plagioclase Al and Ca
221 have positive correlation, whereas Si and Ca have negative correlation (**Supplementary Fig. 1**).
222 Thus, for Si and Ca the covariance matrix for transformed parameters is significantly different for
223 plagioclase and amphibol .
224
225 Using just three elements (Si-Ca & Al-Ca) we can therefore distinguish all five discrete components
226 in SK394A by assessing the pairwise combinations of clusters that exist (**Table 1**). Nonetheless, by
227 using just three elements we are unable to distinguish all mixed pixels. For example, the plagioclase
228 phenocryst at the bottom left of sample SK394A contains many mixed pixels due to the presence of
229 both cracks and melt inclusions (**Fig. 1b**). Using only Si-Ca and Al-Ca, however, these cracks and
230 voids are composed of a mixture of components whose composition is most similar to amphibole.
231 To resolve this we increase the number of possible NMC-NFC combinations. Resultantly, the
232 number of unique combinations of NMC-NFC clusters increases (**Table 2; Supplementary Fig. 2**).
233
234 To assess which unique combinations represent phenocryst phases we identify those that have at
235 least one pixel that is entirely surrounded by pixels of the same unique combination. The
236 assumption here is that in a 3x3 grid, if all pixels have the same unique combination of clusters the
237 central pixel cannot be a mixed pixel [*central pixel assumption*]. As we increase the number of

possible combinations of NMC and NFC, mixed pixels will be distinguished from phenocryst pixels and less likely to satisfy the central pixel assumption. Thus, the results are more likely to converge to the true solution and mixed pixels will be removed. Care must be taken, however, when using elements that are in low concentrations in all components, and close to the instrumental detection limit (e.g. Ti, Cr, Mn). Such elements will likely introduce noise into the phenocryst phases and so the results will not converge to the true solution (**Supplementary Fig. 3**). There is a computational cost to the increased number of NMC-NFC combinations. For a single map (500 x 500 pixels) the phase classification algorithm took 154.4 seconds to process the 11 combinations in **Table 2**, using a 4GHz i7 processor with 16GB RAM.

In some cases the finite mixture model will not converge for particular combinations of elements (**Supplementary Table 1**). In these scenarios care must be taken when choosing the final combinations of elements classify phases. If the finite mixture models are not converging, it is possible to change the parameters of the flexmix model. For example, increasing the number of iterations the EM algorithm can run for, or running the EM algorithm repetitively for either different numbers of latent class components (Leisch, 2004). Such an approach could possibly help the finite mixture model convergence to a global maximum, in examples where not all phases have been properly classified (**Fig. 2b**). Such changes, however, would require manual editing of our code.

In our example we use 11 combinations of elements to classify the mineral phases in our thin sections (**Table 2; Supplementary Fig. 2**). After we perform the central pixel assumption we are left with 8 groups, of which 3 groups represent mixed pixels, which we classify as matrix (**Supplementary Fig. 4**). SEM imaging of the matrix reveals microcrystals of clinopyroxene (Cpx), which is not present as a phenocryst phase. Thus, it is possible that small clinopyroxene crystals are creating a chemically discrete group within the matrix and dominate one of the 3 groups of mixed pixels. To generate maps such as in **Figure 1**, it is up to the user to allocate each of these unique clusters to a mineral phase, matrix, or vesicles, based on optical microscopy and the maps of raw element counts. It is possible for one mineral phase to be represented by two groups, especially when the data is clearly separated into multiple discrete solid solution members (e.g., albite and anorthite in plagioclase). The final phase maps are presented in **Figure 1** for SK394A and SK394C.

2.2 Segmentation

Once individual crystals have been classified, we use a segmentation algorithm combining a simple linear iterative clustering (SLIC) algorithm and an affinity propagation (AP) clustering algorithm (Frey & Ducek, 2007; Achanta et al., 2012; Zhou, 2015). The SLIC algorithm was originally developed to perform image segmentation of optical images, where the composition of a pixel is represented in a colour space such as RGB or CIELAB. The principle of the SLIC method is to identify spatially constrained regions of multiple pixels that share similar characteristics. Each one of these regions is known as a superpixel.

The segmentation algorithm is performed iteratively on each individual crystal, which is extracted as a polygon from the phase map. We choose plagioclase as it is present and abundant as phenocrysts in both samples, and exhibits clear chemical zonation. In this example, we take all crystals that have an area that is larger than 81 pixels (**Fig. 1b-c**). We choose this area as it is equivalent to a 3x3 grid of superpixels, where the centroids are initiated every 3 pixels (see explanation below). For each crystal we extract a rectangular matrix with pixels that belong to one of the following two masks:

- Mask 1: Pixels that lie outside the boundary of the crystal or pixels that do not represent the mineral phase being analysed.
- Mask 2: Pixels that lie within the boundary of the crystal and represent the mineral phase

For all pixels within mask 2 we normalise the measured chemical intensities between zero and one. For all other pixels belonging to mask 1 we set their value to -99 (**Fig. 3**).

SLIC is an iterative algorithm where the centroid of each superpixel is updated repeatedly until convergence is achieved. In our case, the centroid is calculated as the median value of the spatial coordinates and chemical intensities of all pixels with the same superpixel label (l). As we are focusing on plagioclase, the chemical intensity is based on Ca and Na, which are the two major mobile cations present in our samples (**Supplementary Fig. 1**).

To initiate the algorithm, centroids are positioned in a regularly spaced grid within the rectangular matrix (**Fig. 4a**). The spacing of the centroids is determined by the parameter *S*, which represents the numbers of pixels between each centroid. The user can choose the value of the parameter *S*, but the default value works well for crystals of different size and shape. The default value of *S* is calculated using the following equation:

$$S = 2^{log_{10}[nr \cdot nc]-1} \quad \textbf{(3)}$$

where *nr* is the width and *nc* is the height of the rectangular matrix in which the segmentation is performed for the respective crystal. The value of S is rounded to the nearest integer, and the minimum value it can be is 3.

To ensure the algorithm converges and that superpixels are not seeded on noisy pixels, we move the centroids to the lowest average gradient position in all chemical intensities within a 3 by 3 grid (**Fig. 4b**). Furthermore, to aid segmentation of the crystal phase (pixels in mask 2), we force all pixels belonging to the mask 1 to have a value of -99. All initial centroids that lie on a boundary between pixels belonging to mask 2 and pixels belonging to mask 1 will therefore be forced to initiate within the crystal phase (e.g., i in **Fig. 4b**). Finally, we remove duplicate centroids, which will be more likely to occur in smaller crystals.

Once the centroids have been initiated the algorithm is run iteratively. For each iteration, within a $1.5S \times 1.5S$ grid around each centroid, the algorithm calculates a spatial-chemical distance between each pixel and the respective centroid (**Eq. 4**), in which M is used to weight the relative importance of spatial proximity (**Eq. 5**) versus chemical similarity (**Eq. 6**), where *x* and *y* are the coordinates of the pixel, and *C* represents the concentration for all chosen elements. The user can choose the value of *M*, but the default value works well for crystals of different size and shape (**Eq. 7**) given that chemical intensities are normalised between 0 and 1.

$$D = \sqrt{dc^2 + M^2 \cdot (ds/S)^2} \quad \textbf{(4)}$$

$$d_s = \sqrt{(C_k - C_i)^2} \quad \textbf{(5)}$$

$$d_c = \sqrt{(x_k - x_i)^2 + (y_k - y_i)^2} \quad \textbf{(6)}$$

$$M = 2S/(nr + nc) \quad \textbf{(7)}$$

By using the finite mixture model approach to classify the different phases we are confident that this range represents the true chemical range of only the phase we are analysing (in our case plagioclase). The inclusion of additional noisy (i.e., mixed) pixels at this stage would reduce the

efficacy of the segmentation. However, as a safeguard we describe below an additional step to further reduce the influence of noisy pixels on the results of the segmentation.

For an individual pixel, when the value of D is smaller than the value in the previous iteration, its label is updated to the index of the superpixel centroid around which the algorithm is currently searching. The algorithm is iteratively repeated 10 times (**Fig. 5a**), which is long enough to enable convergence in SLIC algorithms (Achanta et al., 2012). The user can modify the number of iterations. Finally two post-processing steps are performed. The first removes single pixels whose label is not identical to at least one other adjacent pixel in either the X or Y dimensions. The second step combines duplicate labels that may have converged onto the same centroid. Each label is represented by a single centroid (**Fig. 5b**), although it is possible for one superpixel to be split across the image (**Fig. 5c**).

Once an image has been segmented into superpixels the next step is to group similar superpixels together to segment the chemical map. The approach we use here is based on the SLICAP algorithm (Zhou, 2015), which uses an affinity propagation (AP) algorithm (Frey & Dueck, 2007). The advantage of the AP algorithm is that it does not require the user to specify the number of clusters. To perform this step we use the *APCluster* package in the R language (Bodenhofer et al., 2011).

Using the AP algorithm, we compare the mean value for all chemical elements of each pairwise combination of superpixels (C_i, C_k) to calculate a negative similarity matrix using the following equation:

$$s_{i,k} \sim \sum -(C_i - C_k)^2 \qquad \textbf{(8).}$$

This similarity matrix forms the basis for a series of transformations. Prior to these transformations, however, is the only semi-subjective step of the AP algorithm, which is to define the values for the diagonal of the similarity matrix. Based on **Eq. 8**, the diagonal values will be zero, which will encourage the AP algorithm to converge to the maximum number of clusters. To avoid over-fitting the number of clusters, however, the diagonal values can be set to a value between the minimum of the non-infinite values in the similarity matrix and zero. In our methodology we set the diagonal values of the similarity matrix to equal a percentile value of the distribution of non-infinite values. To reduce the influence of pixels that do not belong to the crystal (e.g., cracks) we set all pixels in masks 1 to NA. We also remove from the similarity matrix superpixels that contain more

than 90% pixels belonging to mask 1. This is to ensure that noisy pixels belonging to mask 2 (which will make up less than 10% of a superpixel) do not bias the AP algorithm. The prevalence of such superpixels (i.e., containing a few noisy pixels) will depend on how individual phases were classified. Using the finite mixture model presented above we see very few noisy superpixels in our results.

The sensitivity of the results of the AP algorithm to the percentile value (q) will depend upon the aspect ratio and size of the crystal (**Supplementary Fig. 5**). Consequently, we estimate q using the following equation,

$$q = exp^{-q1-q2+q3} \quad \textbf{(9),}$$

where *q1* is calculated as the ratio of the long and short axes of the ellipse,

$$q1 = X_{long}/X_{short} \quad \textbf{(10),}$$

q2 is the area of the large phenocryst (A_{max}) relative to the area of the current phenocryst (A_n),

$$q2 = \ln(A_{max}/A_n) \quad \textbf{(11),}$$

and *q3* is a constant that can be changed to set the maximum (q_{max}) value of q,

$$q3 = \ln(q_{max} + q1_{min} + q2_{min}) \quad \textbf{(12),}$$

where $q1_{min}$ and $q2_{min}$ both equal 1. In our example we set the value of *q3* to 1, such that the q_{max} equals 0.05. A final post-processing step is performed where each of the pixels is allocated to one of the clusters identified by the AP algorithm, and all pixels belonging to mask 1 are set to NA. Pixels belonging to superpixels that contain more than 90% pixels belonging to mask 1 are set to NA, but any individual pixels within this group that belong to mask 2 are attributed to the AP cluster value of neighbouring pixels. The result is a single segmented crystal that is texturally correct (**Fig. 6**), but not yet directly comparable to zonation in other samples and crystals.

2.3 Correlation

Once all crystals have been through the segmentation process we compare the chemical composition of each segmented zone, using the elements that were used to segment the crystals. Rather than compare the average composition of each zone, we have decided to compare both the absolute value and variability of the chemistry in each zone. To do this we compare the mean distance (d_{mean}) in the cumulative probability distribution for a single chemical parameter (**Fig. 7**). This allows us to compare the shape of the distribution, as well as the absolute values.

When using multiple elements there are two approaches: (1) calculate d_{mean} for each element separately and then calculate the average d_{mean} for all elements; or (2) convert the data into a single chemical parameter (e.g. ratio) and calculate a single mean distance. Given we have focused on solid solution zonation in plagioclase between albite (Na) and anorthite (Ca), it is reasonable to calculate d_{mean} for the ratio of these two end members.

As we stated earlier, for samples measured using the same analytical conditions the user may directly compare the raw elemental intensities. Otherwise the intensities will need to be standardised to a quantified unit such as weight percent (wt. %) or atoms per formula unit (apfu). To quantify an elemental map a series of standardised analytical points need to be measured. Ideally, these analyses should be made during the same analytical session in which the elemental map was measured. This would ensure that the reference frame of the elemental map and analytical points is identical, and will make calibration easier (e.g., Lanari et al., 2014).

To correlate the segmented zones in our example we calibrate Ca and Na counts in each sample for their respective atoms per formula unit (apfu) (**Supplementary Fig. 6; Supplementary Table 2**), which we in turn use to calculate the approximate anorthite content of the plagioclase in mol. % using the following equation,

$$An = 100 \cdot \left(\frac{Ca^{2+}}{Ca^{2+}+Na^{2+}}\right) \qquad \textbf{(13).}$$

We compare the cumulative probability distribution of anorthite for each zone, across the complete range of anorthite present in the two samples, and calculate d_{mean}. We plot the results as a distance matrix, and using hierarchical clustering we identify groups of geochemically similar zones (**Fig. 7-8**). We define these as zoning groups, which are correlated across crystals and samples, and which form the chemical building blocks of each crystal.

3. Results & Discussion

The segmentation algorithm splits each phenocryst into a number of different zoning groups based on the anorthite composition of each crystal. In sample SK394A we analysed 29 phenocrysts, in which we identified 1-3 distinct zoning groups per crystal (**Fig. 9a**). In sample SK394C we analysed 28 phenocrysts, in which we identified 1-3 distinct zoning groups per crystal (**Fig. 9b**). Across both samples we identified 90 (48 + 42) distinct zones in total, which correspond with anorthite composition (**Fig. 9c,d**).

A key aspect of correlating crystal zones for the proposed method is the distance matrix (**Fig. 7)**, which allows quantitative comparison of zoning chemistry between samples. The number of final zoning groups can be guided by a qualitative analysis of the distance matrix (**Fig. 7c**), where pairwise combinations of zones are combined so that they have similar [low] values of d_{mean}. The number of zoning groups can also be informed by scoring metrics such as the c-index (**Fig. 7b**; Hubert & Schultz, 1976). The c-index is a relatively simple scoring metric that compares the within-cluster pairwise distances and the within-sample pairwise distances. As the value of the c-index decreases, the number of zoning groups is defined as better describing the data. As you can see in **Figure 7b**, this would suggest that the best number of groups is 25. This is clearly an over-fitting of the data and is a result of the hierarchical structure of the clustering algorithm. Whenever using a scoring metric such as this it is important to interpret the structure of the results, not only the absolute value of the metric. Hence, we base our assessment of the number of groups on identifying the first major plateau in the c-index score.

Choosing six zoning groups ensures that crystals that are segmented into two zones or more (**Fig. 9a-b**) also contain two or more zoning groups (**Fig. 8a-b**). Alternatively, we could choose five zoning groups instead of six, which will result in some crystals segmented into two or more zones containing only a single zoning group (**Supplementary Fig. 7**). Based on the distance matrix plotted in **Figure 7c**, this would mean that the red and yellow zoning groups would be combined. At this stage we can observe the success of the segmentation and correlation algorithms, as fragments belonging to the same crystal are attributed to identical zoning groups.

Irrespective of whether we choose five or six zoning groups, the chemical data can be interpreted in a very similar way. All zoned crystals exhibit a rim composition represented by the yellow or red

zoning group (**Fig. 8a-b**). The presence of this common rim in both samples supports the observation that they are contemporaneous and erupted in the same magma. Of these zoned crystals, the majority in both samples are normally zoned, although a few crystals are also reversely zoned. Most core compositions belong to light blue zoning group, which is present in both samples and represents the majority of normally zoned crystals (**Fig. 8a-b**). A second pink zoning group, is also present in both samples (**Fig. 8a-b**). It has the lowest An# compositional range (**Fig. 8c**) and is most common as a core, in what are therefore reversely zoned crystals. A third green zoning group represents cores that are only present in the scoriacious sample (**Fig. 8a**). This group of cores has a distinctly high An# compositional range (**Fig. 8c**), indicating crystals that are sourced from a deeper, hotter and more volatile-rich portion of the magmatic system (Sisson & Grove, 1993; Melekhova et al., 2017). Finally, a dark blue zoning group that mantles one of these high-An cores in SK394A, is also present in one fragmented crystal in SK394C that displays patchy zonation.

The maximum number of zones identified within an individual crystal will depend on two main factors: (i) the spatial resolution of the chemical map versus the sizes of crystals; and (ii) the average size of superpixels, which will be a function of the parameter S. The choice of analytical conditions will be determined by the research question that is being investigated. However, given that the minimum value of S can be 3, we suggest that the optimum resolution be set at approximately 1/3 of the smallest feature targeted for segmentation. At these highest resolutions, the image will likely be segmented into more superpixels than necessary. However, whilst this may be computationally inefficient, it will not lead to over-segmentation, which will be limited by both the affinity propagation and hierarchical clustering that follows. For example, if we considered the results in **Figure 9a-b** to be over-segmented, by choosing only five instead of six zoning groups, the complexity in the segmentation is reduced in the finally correlated crystals (**Supplementary Figure 7**). Finally, the affinity propagation can be optimised by the parameter *q3* (**Eq. 12**) to alter the complexity of the zoning that is segmented.

To this point we have focussed solely on the spatial resolution and its influence on the segmentation results. The chemical resolution, however, will also influence the efficacy of both the phase classification and segmentation. Again, the chemical resolution that is required will be influenced by the mineral phases and the chemistry (e.g., major vs trace) of the zoning that is of interest. Ultimately, a judgement will be required between spatial resolution, chemical resolution and mapping extent. For example, as we were interested in mapping a large area ($1cm^2$) with medium resolution (20μm) we decided that the WDS detector on an EPMA would provide the

optimum chemical resolution for classification and segmentation. However, the development of more sensitive silicon drift detectors will facilitate higher precision chemical mapping at larger spatial extent and higher spatial resolutions using both x-ray spectrometry and electron spectroscopy.

In porphyritic rocks, such as the samples presented in this manuscript, the matrix can represent a large proportion of the total mapped area. Consequently, unless the spatial resolution of the imaging method is extremely high (~a few μm) the resulting image will be dominated by a mixed signal. We can observe the effect of this by comparing the results of our new approach for classifying mineral phenocryst phases with both unsupervised and supervised k-means clustering. The results show our proposed method is most compatible with what we observe under a petrographic microscope, including the distribution and abundance of cracks and inclusions and crystal shape.

K-means clustering is an iterative algorithm that separates data into distinct clusters, by classifying each multivariate data point to the cluster that has the nearest mean value. In the unsupervised approach only the number of cluster centres is chosen, whereas in the supervised approach the value of each centre is initiated prior to running the algorithm. In our case, we choose six clusters, which equates to the number of distinct components in SK394A, including mixed pixels and vesicles (**Fig. 1b**). In the supervised approach, we define the centre based on the mean average of all points belonging to each distinct component in **Figure 1b**. We run both versions of the algorithm for the five elements used in the finite mixture model (**Table 2; Fig. 10**), although the results are similar when we use all 10 oxides that were measured using the WDS detector during the analytical session (**Supplementary Fig. 8**).

The first impact of the porphyritic nature of the samples can be seen in both k-means approaches (**Fig. 10a-b**), in which amphibole has not been distinguished from orthopyroxene, even in the supervised approach. This is because these two phases are more similar in composition than variability within the mixed pixels, especially given that the matrix contains clinopyroxene, which is not present as a phenocryst. Consequently, discrete components identified within mixed pixels and amphibole-orthopyroxene becomes a single cluster. A similar effect can also be seen for oxides and vesicles, although this is resolved using the supervised algorithm. By simply attributing each pixel to the closest centroid, and not running the k-means algorithm we can see that the results are more similar to those in **Figure 1b**, with both amphibole-orthopyroxene and oxides-vesicles correctly

separated (**Fig. 10c**). However, these centroids have been learnt a-priori using our finite mixture model, and would not be available if only relying on a k-means/centroid-based approach.

To the centre right of each image in **Figure 10** is the crystal in **Figures 3-6**, which has not been as efficiently classified compared to the finite mixture model. Large mineral inclusions are removed, but cracks less than 20μm remain allocated as plagioclase, in both the unsupervised and supervised approaches (**Fig. 10a-b**). Based on the centroid approach, these mixed features are better resolved (**Fig. 10c**). However, due to the similarity between the mixed-matrix composition (in which plagioclase dominates) and the rims of many plagioclase phenocrysts, many crystals have only been partially classified as plagioclase. Hence, even if a centroid-based approach is able to classify each of the mineral phases, it will not correctly remove all mixed pixels at the resolution of individual phenocryst. This will influence the efficacy of further analyses, such as the segmentation we have proposed in this manuscript.

4. Conclusions

We have developed a method to optimally segment zoned phenocrysts, based on their chemical composition, at a thin-section scale. This provides a robust approach to distinguish and correlate mineral zonation. We emphasise that the method is semi-autonomous: it requires an understanding of the mineral phases that are present in a sample and the chemical variability that characterises them. The methodology is adaptable to different chemical elements and different spatial scales depending upon the scientific question of interest. In this manuscript there has been a focus on chemical maps, but the segmentation approach could also be calibrated for use with the results of imaging techniques such a cathodoluminescence or backscatter electron.

Our approach is based on a 3-step procedure: (i) the classification of mineral phases; (ii) segmentation of intra-crystal zonation; and (iii) correlation of inter-crystal zonation. Independently, the first classification step provides a method for the separation of mineral phases. Additionally, the results of the second step will be useful for the quantification of crystal fracturing and other physical parameters describing mineral textures (Higgins et al., 2021).

The methodology has been applied to plagioclase phenocrysts in 1cm^2 thin section maps from two contemporaneous samples. The results show all crystals share a common rim composition,

supporting the hypothesis that both samples were erupted in the same magma. A small number of high-An# plagioclase cores are exclusively found in the scoriaceous sample, which could indicate a possible role of magma origin on the fragmentation efficiency in the shallow conduit.

The classification of mineral phases using a finite mixture model has wide application in many different fields of geology and geoscience. It provides an effective way to deal with noisy data associated with mixed pixels. By removing mixed pixels, down-stream analyses will be significantly improved, such as the segmentation we propose in this manuscript. The segmentation of crystals has wide application in a variety of mineral sciences, beyond igneous geochemistry and petrology. This approach will allow the fingerprinting of individual crystals (e.g., Higgins et al., 2021) and in the future we believe it will be possible to automatically sequence the temporal zoning within a crystal.

Acknowledgements:
TS and OH received funding from the European Research Council (ERC) under the European Union's Horizon 2020 research and innovation program (Grant agreement 677493-FEVER – Prof. Luca Caricchi).

Figure captions:

1. (a) Sample location on the island of St. Kitts; (b+c) Phase maps for samples SK394A and SK394C, classified using the finite mixture model approach developed in this manuscript. All white space is classified as vesicles.
2. Finite mixture model using the transformed parameters in Eq. 1-2 for (a-c) Al-Ca and (d-f) Si-Ca in SK394A. (a,d) The classification of the discrete components (colour) in Fig. 1b, plotted in the transformed parameter space and labelled (shape) according to the results of the finite mixture model. (b,e) The different clusters (colour) identified by the finite mixture model; (c,f) The resulting cluster map according the results of the finite mixture model using the identical colour scheme as panels b and c.
3. Example phenocryst in SK394A: (a) Raw counts of Ca measured using the EMPA, with the outline of the crystal in white according to the results of the finite mixture model; (b) the two masks used to run the segmentation algorithm; (c) normalised counts of Ca in Mask 2.
4. Superpixel centroids (a) at initial position and (b) moved to the lowest gradient position in a 3x3 grid. Pixels may move from their original position because (i) they were located in mask 1, but adjacent to a pixel in mask 2, to which it moves to; (ii) on the edge of the phenocryst and so moves to an interior position; or (iii) moves to a low-gradient position within the crystal.
5. Superpixels and their respective centroids after 10 iterations of the segmentation algorithm. Each of the 80 superpixels is a slightly different colour according to the scale. (a) Locations of superpixel centroids for all 10 iterations. Centroids with lower opacity represent previous locations from where the algorithm has converged. Centroids with a red outline represent a final centroid location. (b) Each superpixel outlined in grey, and it's associated centroid. The white box represents the area covered in panel c. (c) The red boxed outline represents a single superpixel (number 16) that is spatially distributed. This will often occur with areas that belong to mask 1, which can be found within and exterior to the crystal.

6. Phenocryst segmented into two zones based of the results of the affinity propagation algorithm. The superpixels are outlined in grey, and two exemplar pixels from the affinity propagation are outlined in red.
7. Correlation of segmented zones, based on (a) the anorthite distribution. The number of zoning groups is chosen manually based on the results of a hierarchical clustering algorithm, and is informed: by (b) quantitative scoring metrics such as the C-Index; and (c) by visually using a distance matrix. The colours to the right of the distance matrix correspond to zoning groups in Figure 8.
8. Correlation of segmented plagioclase in (a) SK394A and (b) SK394C. Across both samples, six zoning groups have been identified, based on (c) the anorthite composition of each zone. The colour of each of the zoning groups corresponds to that plotted next to the distance matrix in Figure 7.
9. Segmented zones in individual plagioclase, where the colour does not represent the correlation of chemistry. Phenocrysts have been split into a maximum of three zones in both (a) SK394A and (b) SK394C. (c-d) The calibrated anorthite composition of segmented plagioclase in both samples, using Eq. 13.
10. Classification of 6 discrete components in SK394A using the six elements in Table 2. The results are for: (a) an unsupervised k-means; (b) a supervised k-means; and (c) a minimisation of the Euclidean distance to the mean value of each discrete component identified in Figure 1a. The mean values used in panel (c) are used to initiate the supervised approach in panel (b).

Tables:

Table 1: Unique cluster-combinations for the five discrete components in SK394A, using the results from the Al-Ca and Si-Ca discrete mixture models in Figure 3

Component	Index (Al-Ca)	Index (Si-Ca)	Combination
Plagioclase	1	1	1-1
Orthopyroxene	3	3	3-3
Amphibole	1	3	1-3
Oxides	3	2	3-2
Vesicles	2	2	2-2

Table 2: Nine combinations of elements used to discretely cluster sample SK394A

Combination	No. of clusters identified	Cumulative combinations of clusters
Al-Ca	4	4
Al-Fe	3	12
Al-K	4	37
Al-Mg	3	106
Si-Al	4	277
Si-Ca	5	582
Si-Fe	3	747
Si-K	6	1464
Si-Mg	1	1464

Supplementary files:

Supplementary Data (Excel file) – Supplementary tables 1-2
Supplementary Figures (PDF file) – Supplementary figures 1-8

References:

Achanta, R., Shaji, A., Smith, K., Lucchi, A., Fua, P., Süsstrunk, S., 2012. SLIC superpixels compared to state-of-the-art superpixel methods. *IEEE transactions on pattern analysis and machine intelligence*, *34*(11), 2274-2282.

Bachmann, O., Dungan, M. A., 2002. Temperature-induced Al-zoning in hornblendes of the Fish Canyon magma, Colorado. *American Mineralogist*, *87*(8-9), 1062-1076.

Bennett, E. N., Lissenberg, C. J., Cashman, K. V., 2019. The significance of plagioclase textures in mid-ocean ridge basalt (Gakkel Ridge, Arctic Ocean). *Contributions to Mineralogy and Petrology*, *174*(6), 1-22.

Bodenhofer, U., Kothmeier, A., Hochreiter, S., 2011. APCluster: an R package for affinity propagation clustering. *Bioinformatics*, *27*(17), 2463-2464.

Cao, M., Evans, N. J., Reddy, S. M., Fougerouse, D., Hollings, P., Saxey, D. W., McInnes, B.I.A., Cooke, D.R., McDonald, B.J., Qin, K. (2019). Micro-and nano-scale textural and compositional zonation in plagioclase at the Black Mountain porphyry Cu deposit: Implications for magmatic processes. *American Mineralogist: Journal of Earth and Planetary Materials*, *104*(3), 391-402.

Cashman, K., Blundy, J., 2013. Petrological cannibalism: the chemical and textural consequences of incremental magma body growth. *Contributions to Mineralogy and Petrology*, *166*(3), 703-729.

Cheng, L., Costa, F., Carniel, R., 2017. Unraveling the presence of multiple plagioclase populations and identification of representative two-dimensional sections using a statistical and numerical approach. *American Mineralogist*, *102*(9), 1894-1905.

Costa, F., Chakraborty, S., 2004. Decadal time gaps between mafic intrusion and silicic eruption obtained from chemical zoning patterns in olivine. *Earth and Planetary Science Letters*, *227*(3-4), 517-530.

Druitt, T. H., Costa, F., Deloule, E., Dungan, M., Scaillet, B., 2012. Decadal to monthly timescales of magma transfer and reservoir growth at a caldera volcano. *Nature*, *482*(7383), 77-80.

Frey, B. J., Dueck, D., 2007. Clustering by passing messages between data points. *science*, *315*(5814), 972-976.

Ginibre, C., Kronz, A., Wörner, G., 2002. High-resolution quantitative imaging of plagioclase composition using accumulated backscattered electron images: new constraints on oscillatory zoning. *Contributions to Mineralogy and Petrology*, *142*(4), 436-448.

Ginibre, C., Wörner, G., Kronz, A., 2007. Crystal zoning as an archive for magma evolution. *Elements*, *3*(4), 261-266.

Gottlieb, P., Wilkie, G., Sutherland, D., Ho-Tun, E., Suthers, S., Perera, K., Jenkins, B., Spencer, S., Butcher, B., Rayner, J., 2000. Using quantitative electron microscopy for process mineralogy applications. *JOM*, *52*(4), 24-25

Hanchar, J. M., Miller, C. F., 1993. Zircon zonation patterns as revealed by cathodoluminescence and backscattered electron images: implications for interpretation of complex crustal histories. *Chemical geology*, *110*(1-3), 1-13.

Higgins, O., Sheldrake, T., Caricchi, L., 2021. Quantitative chemical mapping of plagioclase as a tool for the interpretation of volcanic stratigraphy: an example from St Kitts, Lesser Antilles. *Earth and Planetary Science Letters* (under review).

Hubert, L., Schultz, J., 1976. Quadratic assignment as a general data analysis strategy. *British journal of mathematical and statistical psychology*, *29*(2), 190-241.

Humphreys, M. C., Blundy, J. D., Sparks, R. S. J., 2006. Magma evolution and open-system processes at Shiveluch Volcano: Insights from phenocryst zoning. *Journal of Petrology*, *47*(12), 2303-2334.

Humphreys, M. C. S., Edmonds, M., Plail, M., Barclay, J., Parkes, D., Christopher, T., 2013. A new method to quantify the real supply of mafic components to a hybrid andesite. Contributions to Mineralogy and Petrology, 165(1), 191-215.

Lanari, P., Vidal, O., De Andrade, V., Dubacq, B., Lewin, E., Grosch, E. G., Schwartz, S., 2014. XMapTools: A MATLAB©-based program for electron microprobe X-ray image processing and geothermobarometry. *Computers & Geosciences*, *62*, 227-240.

Lanari, P., Vho, A., Bovay, T., Airaghi, L., Centrella, S., 2019. Quantitative compositional mapping of mineral phases by electron probe micro-analyser. *Geological Society, London, Special Publications*, *478*(1), 39-63.

Lee, M. R., Martin, R. W., Trager-Cowan, C., Edwards, P. R., 2005. Imaging of cathodoluminescence zoning in calcite by scanning electron microscopy and hyperspectral mapping. *Journal of Sedimentary Research*, *75*(2), 313-322.

Leisch, F., 2004. FlexMix: A general framework for finite mixture models and latent class regression in R. *Journal of Statistical Software*, 11 (8), 1-18.

Maitre, J., Bouchard, K., Bédard, L. P., 2019. Mineral grains recognition using computer vision and machine learning. *Computers & Geosciences*, *130*, 84-93.

Melekhova, E., Blundy, J., Martin, R., Arculus, R., Pichavant, M., 2017. Petrological and experimental evidence for differentiation of water-rich magmas beneath St. Kitts, Lesser Antilles. *Contributions to Mineralogy and Petrology*, *172*(11-12), 98.

Pietranik, A., Koepke, J., Puziewicz, J., 2006. Crystallization and resorption in plutonic plagioclase: implications on the evolution of granodiorite magma (Gęsiniec granodiorite, Strzelin Crystalline Massif, SW Poland). *Lithos*, *86*(3-4), 260-280.

Probst, L. C., Sheldrake, T. E., Gander, M. J., Wallace, G., Simpson, G., Caricchi, L., 2018. A cross correlation method for chemical profiles in minerals, with an application to zircons of the Kilgore Tuff (USA). *Contributions to Mineralogy and Petrology*, *173*(3), 23.

Shcherbakov, V. D., Plechov, P. Y., Izbekov, P. E., Shipman, J. S., 2011. Plagioclase zoning as an indicator of magma processes at Bezymianny Volcano, Kamchatka. *Contributions to Mineralogy and Petrology*, *162*(1), 83-99.

Singer, B. S., Dungan, M. A., Layne, G. D., 1995. Textures and Sr, Ba, Mg, Fe, K, and Ti compositional profiles in volcanic plagioclase: clues to the dynamics of calc-alkaline magma chambers. *American Mineralogist*, *80*(7-8), 776-798.

Sisson, T. W., Grove, T. L., 1993. Experimental investigations of the role of H 2 O in calc-alkaline differentiation and subduction zone magmatism. *Contributions to mineralogy and petrology*, *113*(2), 143-166.

Ubide, T., McKenna, C. A., Chew, D. M., Kamber, B. S., 2015. High-resolution LA-ICP-MS trace element mapping of igneous minerals: In search of magma histories. *Chemical Geology*, *409*, 157-168.

Viccaro, M., Giacomoni, P. P., Ferlito, C., Cristofolini, R., 2010. Dynamics of magma supply at Mt. Etna volcano (Southern Italy) as revealed by textural and compositional features of plagioclase phenocrysts. *Lithos*, *116*(1-2), 77-91.

Wallace, G. S., Bergantz, G. W., 2002. Wavelet-based correlation (WBC) of zoned crystal populations and magma mixing. *Earth and Planetary Science Letters*, *202*(1), 133-145.

Watt, G. R., Wright, P., Galloway, S., McLean, C., 1997. Cathodoluminescence and trace element zoning in quartz phenocrysts and xenocrysts. *Geochimica et Cosmochimica Acta*, *61*(20), 4337-4348.

Weber, G., Arce, J. L., Ulianov, A., Caricchi, L., 2019. A Recurrent Magmatic Pattern on Observable Timescales Prior to Plinian Eruptions From Nevado de Toluca (Mexico). *Journal of Geophysical Research: Solid Earth*, *124*(11), 10999-11021.

Willis, K. V., Srogi, L., Lutz, T., Monson, F. C., Pollock, M., 2017. Phase Composition Maps integrate mineral compositions with rock textures from the micro-meter to the thin section scale. *Computers & Geosciences*, *109*, 162-177.

Wilson, N. C., MacRae, C. M., 2005. An automated hybrid clustering technique applied to spectral data sets. *Microscopy and Microanalysis*, *11*(S02), 434-435.

Zellmer, G. F., Sparks, R. S. J., Hawkesworth, C. J., Wiedenbeck, M., 2003. Magma emplacement and remobilization timescales beneath Montserrat: insights from Sr and Ba zonation in plagioclase phenocrysts. *Journal of Petrology*, *44*(8), 1413-1431.

Zhou, B., 2015. Image segmentation using SLIC superpixels and affinity propagation clustering. *Int. J. Sci. Res*, *4*(4), 1525-1529.

Figure1

Click here to access/download;Figure;Figure1.jpg

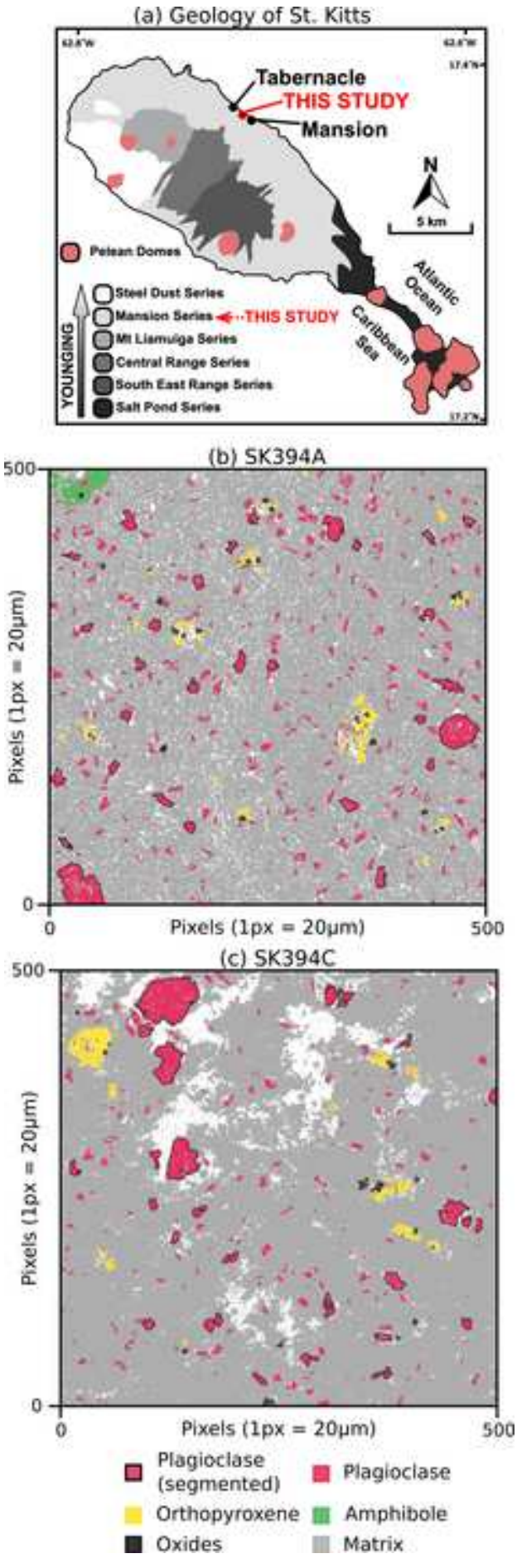

Figure2

Click here to access/download;Figure;Figure2.jpg

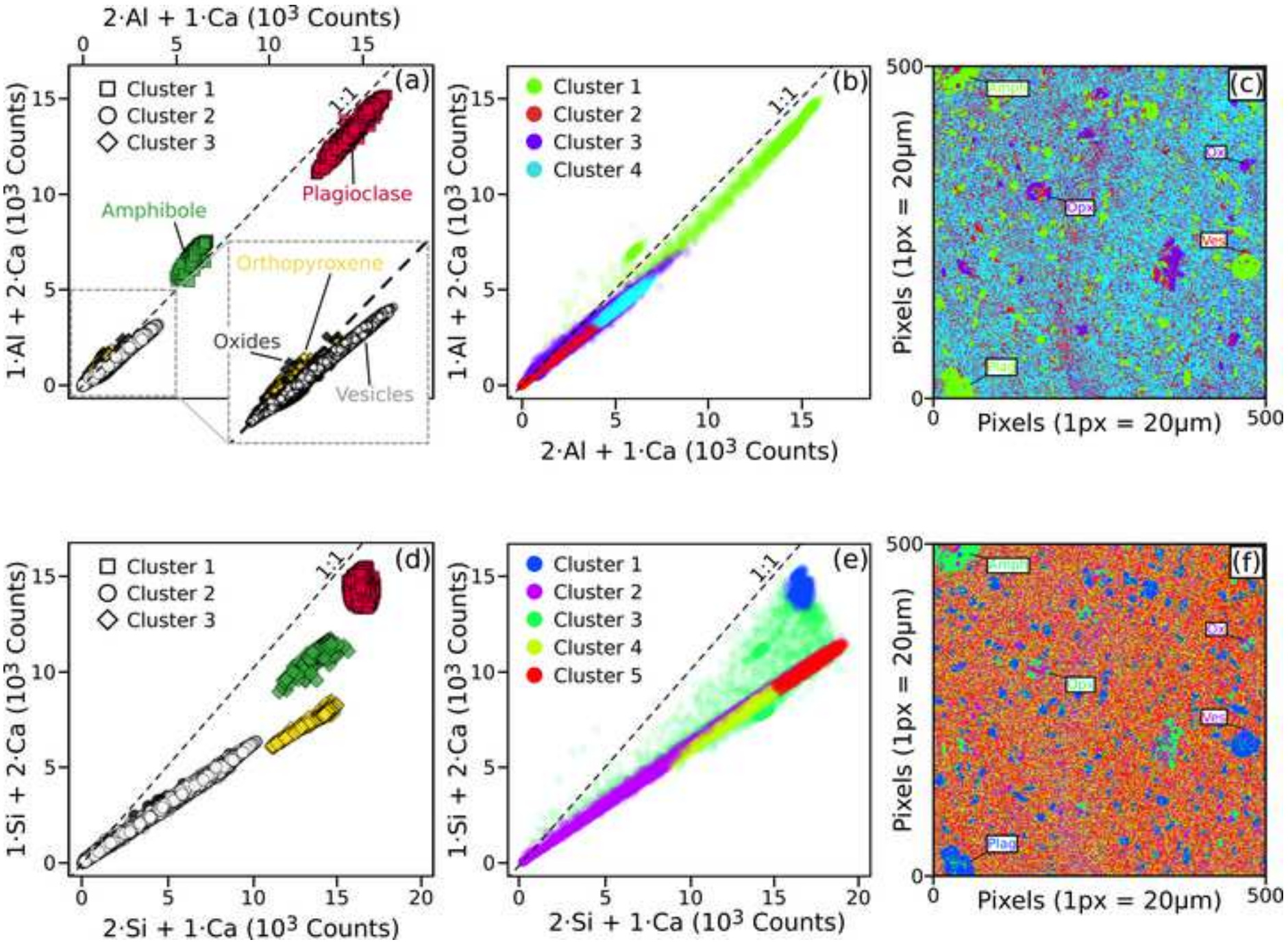

Figure3

Click here to access/download;Figure;Figure3.jpg

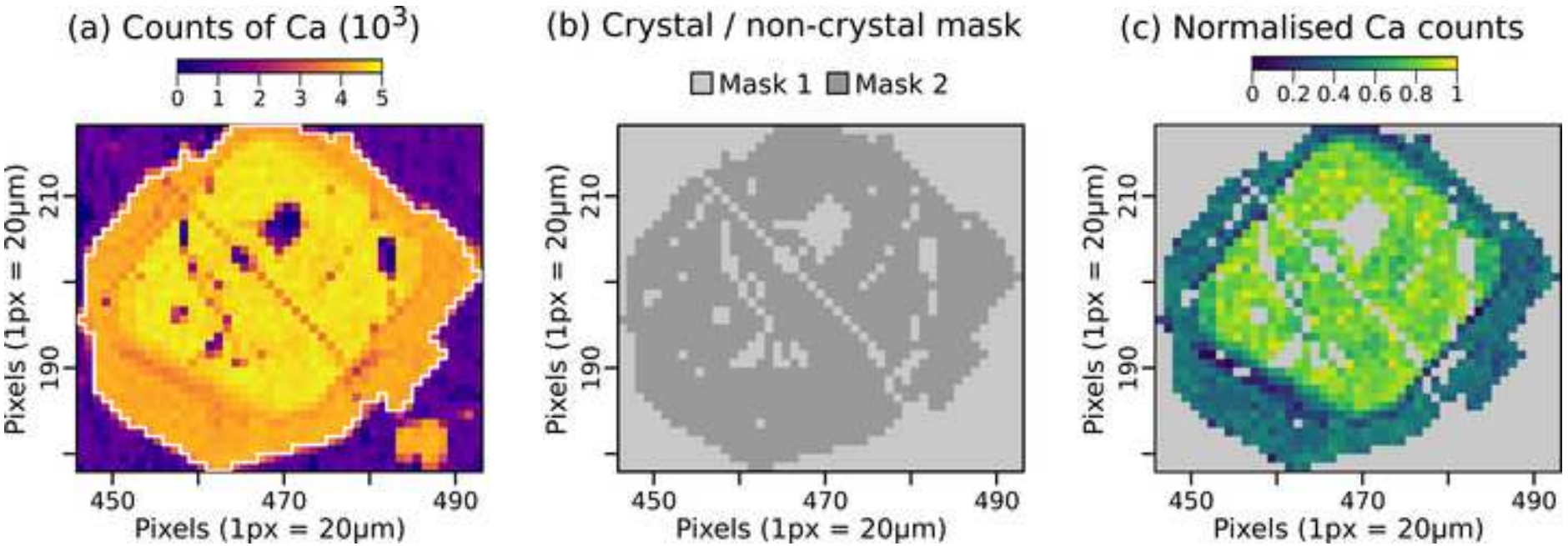

Figure4

Click here to access/download;Figure;Figure4.jpg

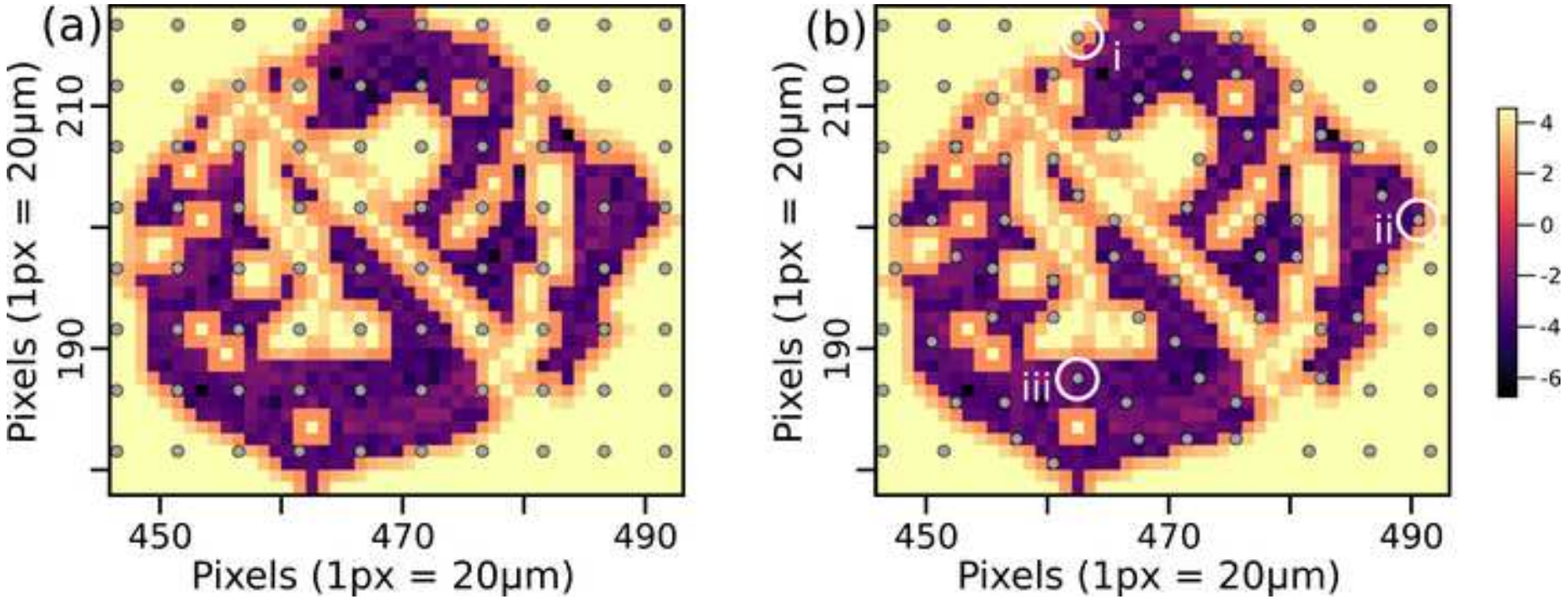

Figure5

Click here to access/download;Figure;Figure5.jpg

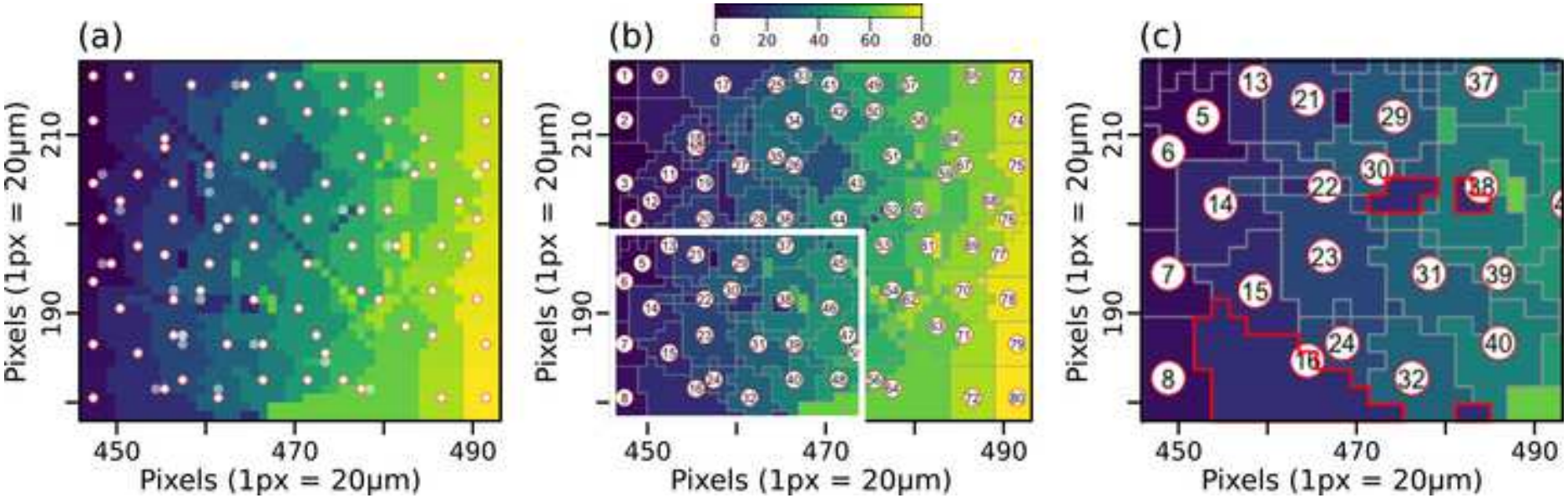

Figure6

Click here to access/download;Figure;Figure6.jpg

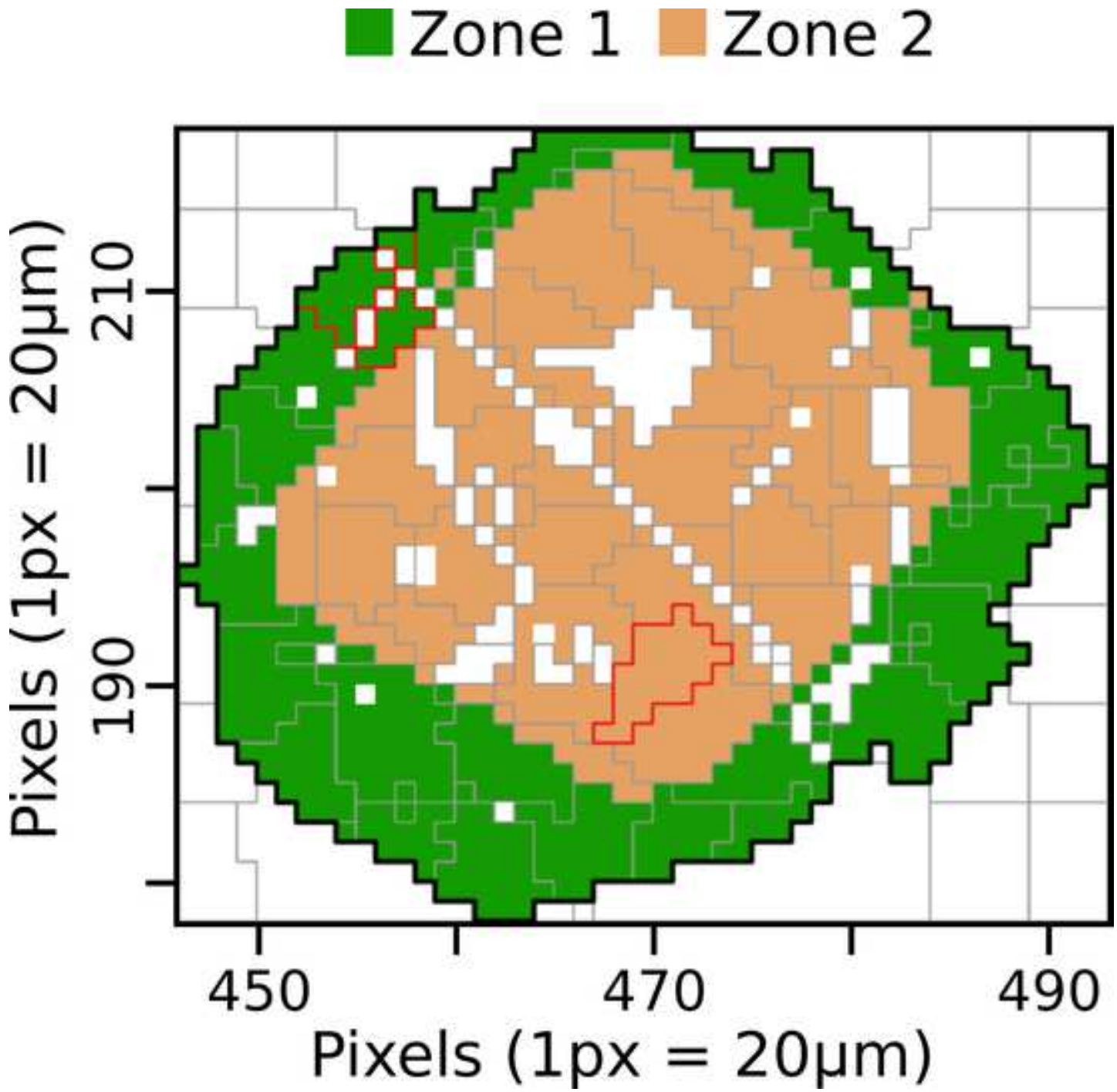

Figure7

Click here to access/download;Figure;Figure7.jpg

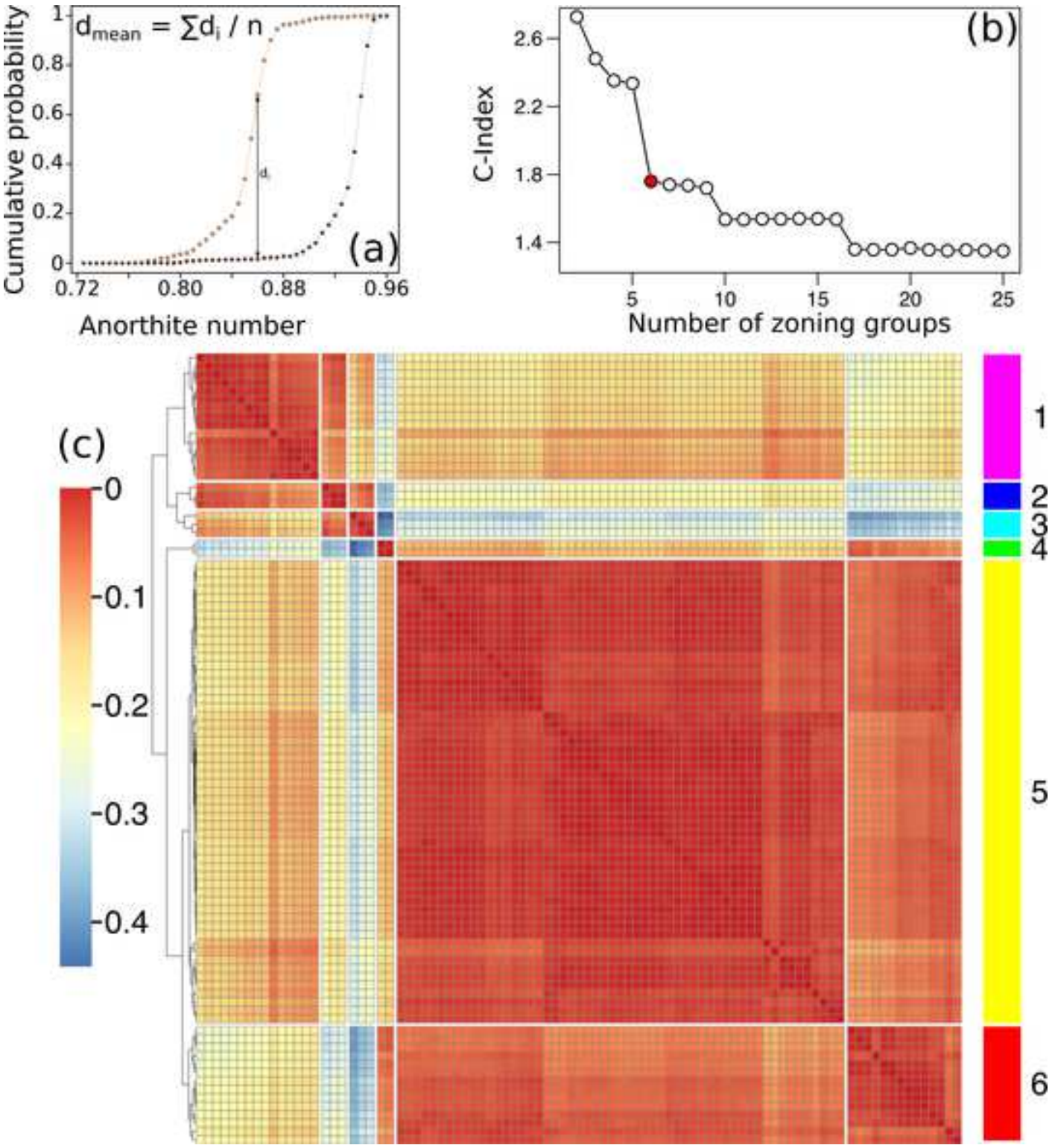

Figure8

Click here to access/download;Figure;Figure8.jpg

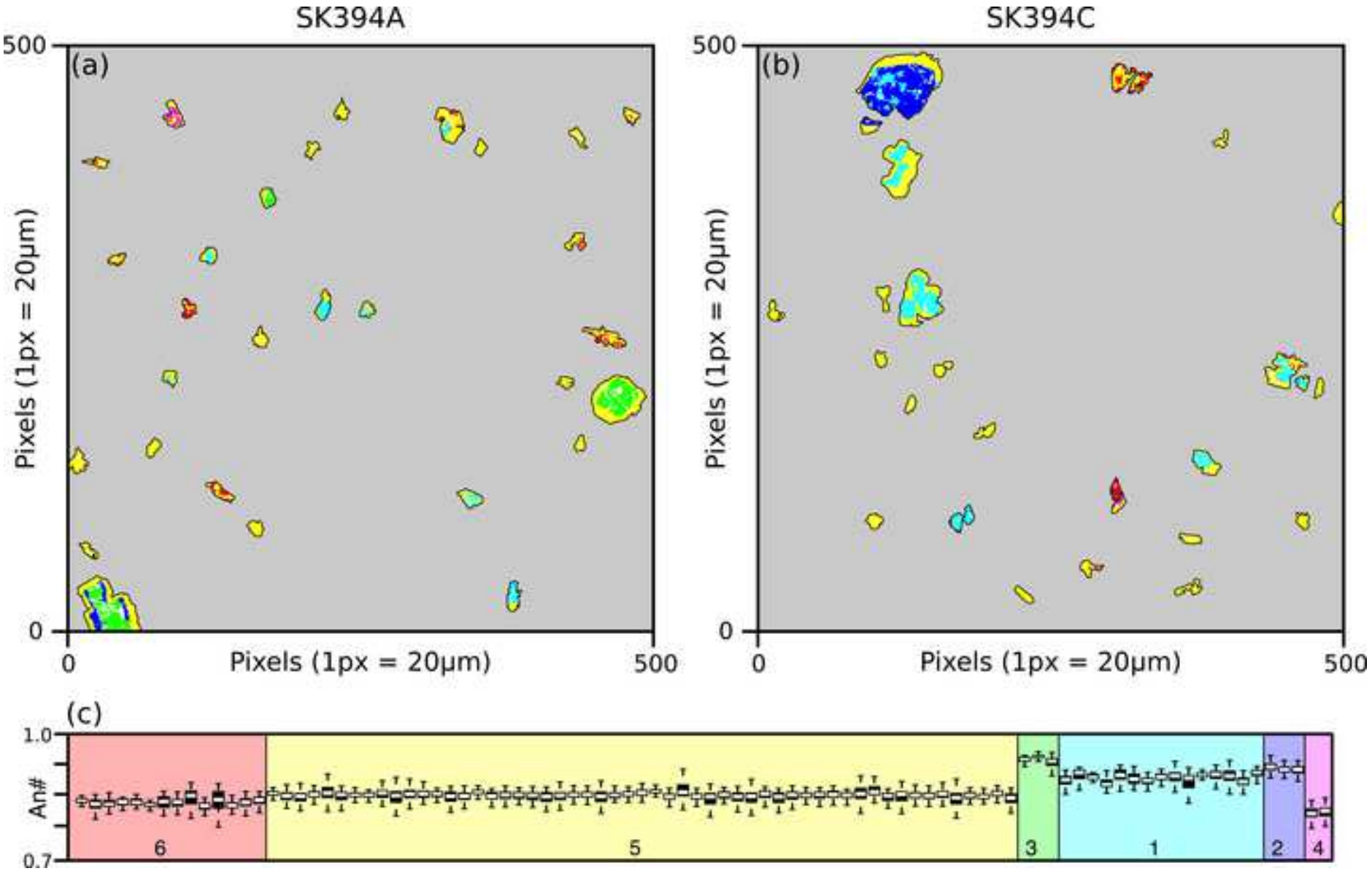

Figure9

Click here to access/download;Figure;Figure9.jpg

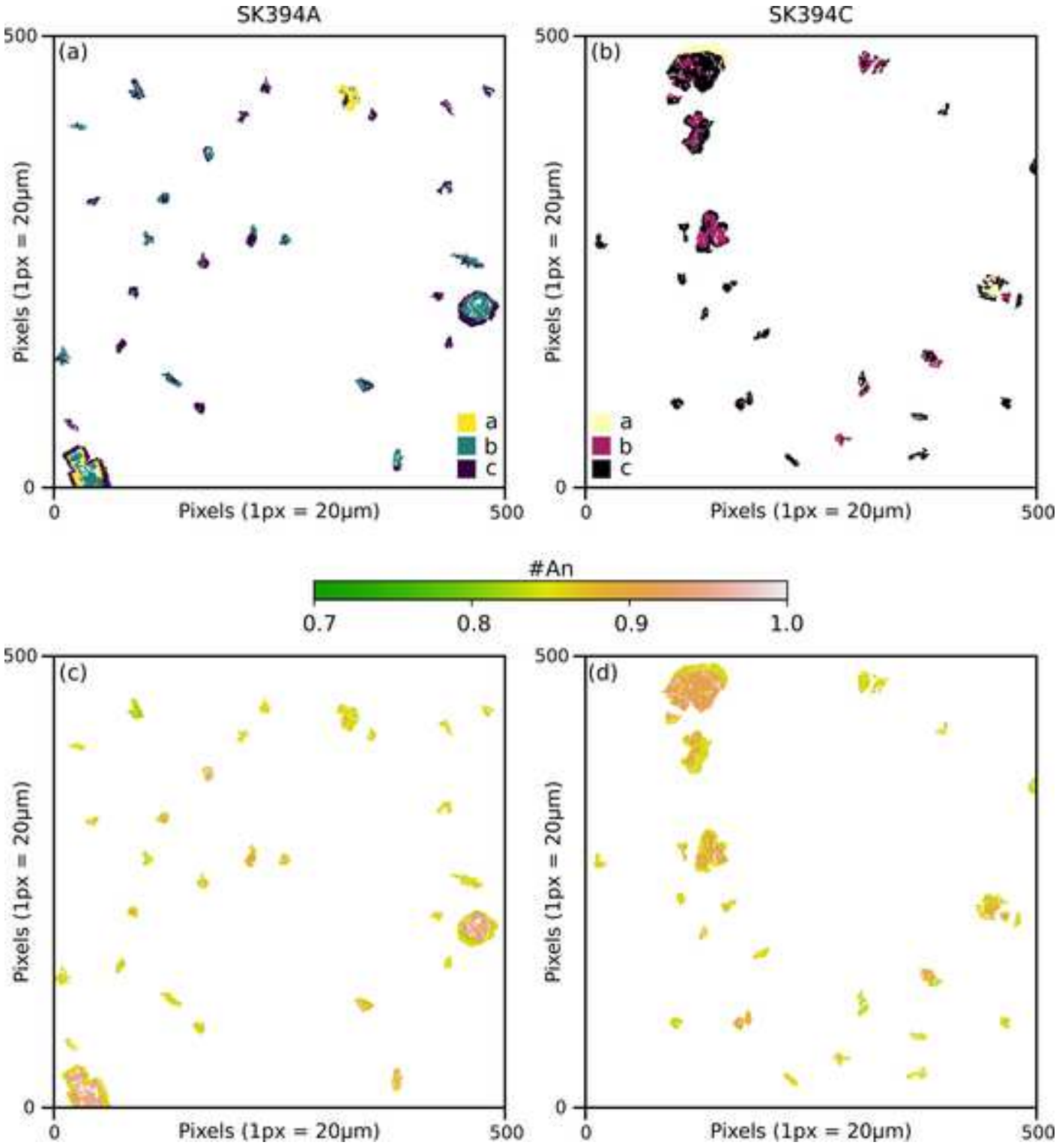

Figure10

Click here to access/download;Figure;Figure10.jpg

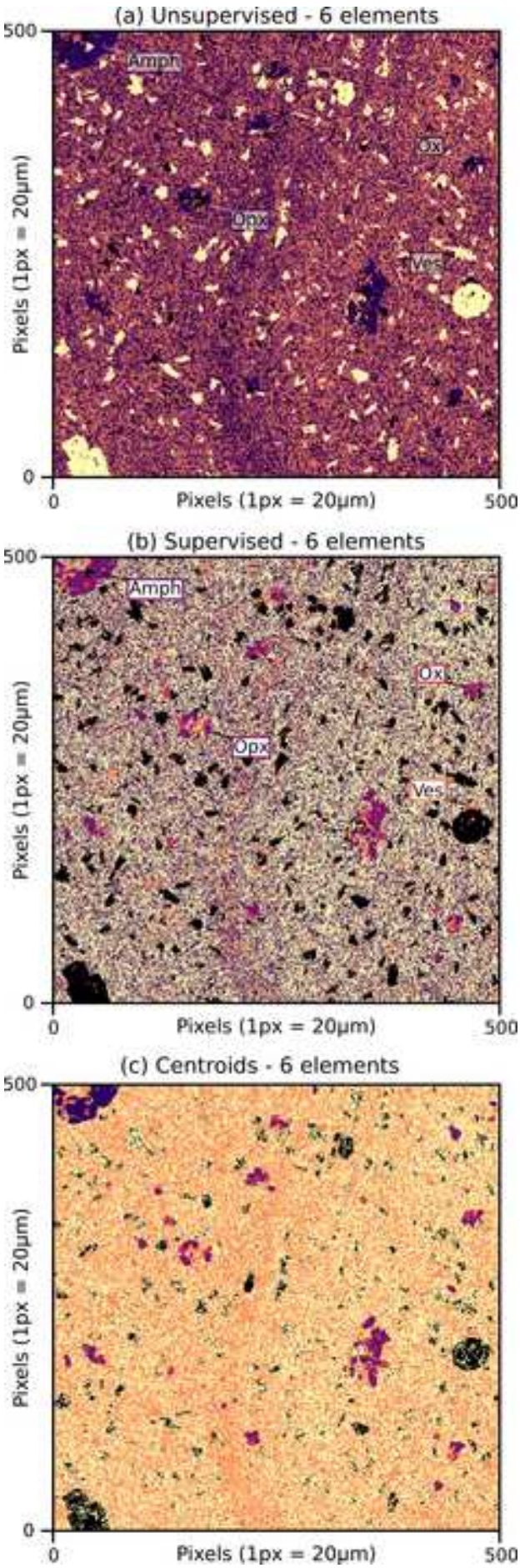

Supplementary Figures (PDF file)

Supplementary figures 1-8

Fig. S1: Plagioclase systematics. Ternary diagram of the three plagioclase-feldspar endmembers (Albite, Orthoclase & Anorthite). Positive correlation of atoms per formula unit between Al & Ca. Negative correlation of atoms per formula unit between Al & Si.

Fig. S2: Results of the individual finite mixture models for all combinations of elements in Table 2.

Fig. S3: Finite mixture model classification for (a-b) Si-Cr, and (c-d) Al-Cr. Segmented plagioclase are outlined in dark grey. Phases are only identified when there is significant variability in the network forming cation. Cr has no influence on the results of the finite mixture model.**Fig. S4:** The eight final discrete components that satisfy the *central pixel assumption* in SK394A.

Fig. S5: Results of the affinity propagation for different percentile values ($1/2^{th}$, $1/4^{th}$, $1/20^{th}$, $1/100^{th}$). You can see that for high percentile values the AP algorithm can segment the crystals into many zones, even over-fitting large crystals (e.g., i & ii). Higher percentile values can provide more information on crystal structure (e.g., iii – here the low Ca region in Figure 3 is identified), but may still over-segment noisy crystals (e.g., iv). Choosing too low values will reduce the number of potential zones, especially in larger crystals (e.g., v).

Fig. S6: Calibration of Si, Al, Ca, Na & K in plagioclase for the chemical maps. Outliers in red have been identified using the Cooks distance, and are not included in the calibration.

Fig. S7: Correlation of phenocryst zones when the results of the hierarchical clustering are split into five groups.

Fig. S8: Classification of 6 discrete components in SK394A using: (a) unsupervised k-means; (b) supervised k-means; and (c) a minimisation of the Euclidean distance to the mean value of each discrete component identified in Figure 1a. The mean values used in panel (c) are used to initiate the supervised approach in panel (b). All ten measured oxides have been used.

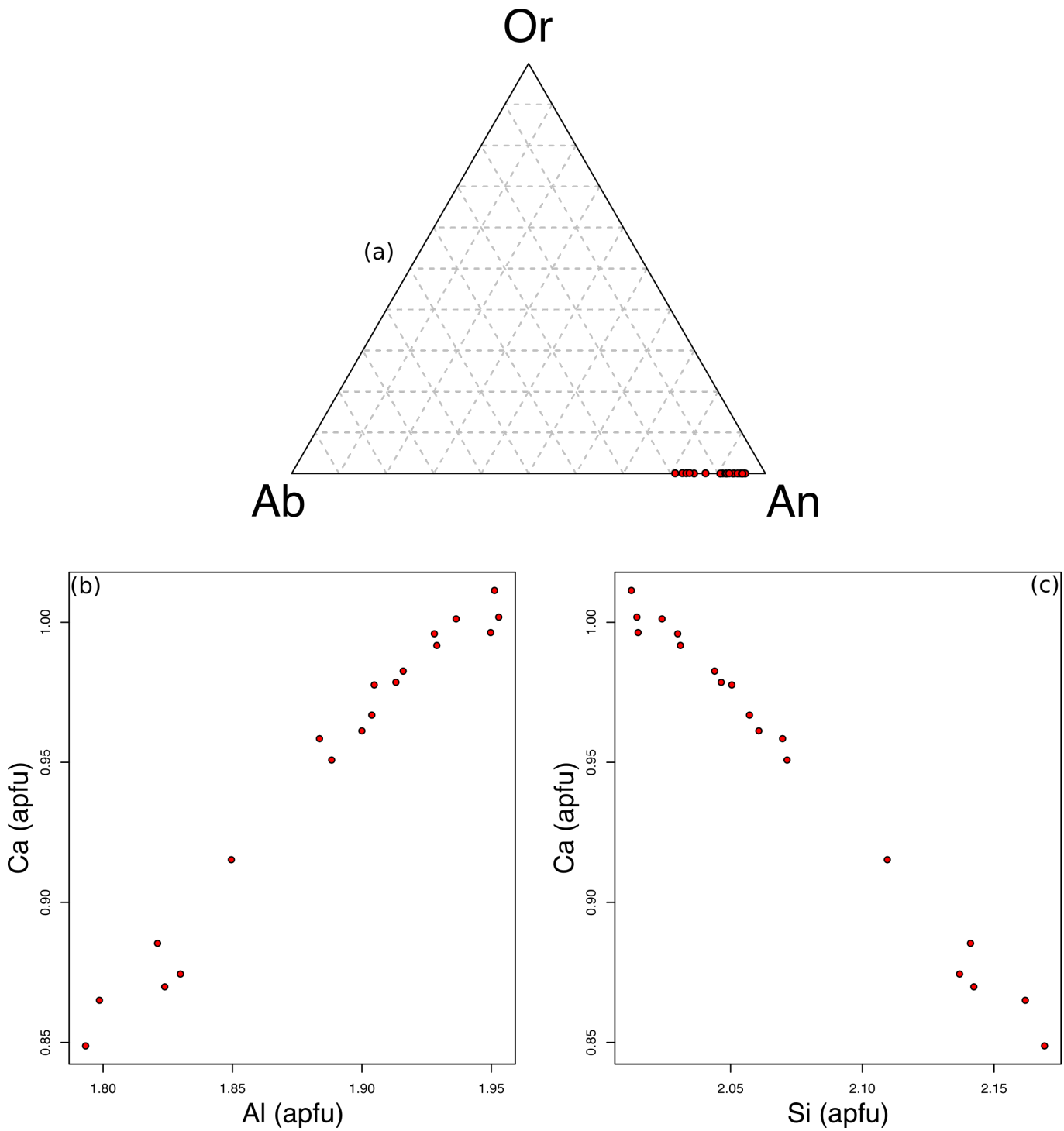

Fig. S1: Plagioclase systematics: (a) Ternary diagram of the three plagioclase-feldspar endmembers (Albite, Orthoclase & Anorthite); (b) Positive correlation of atoms per formula unit between Al & Ca; (c) Negative correlation of atoms per formula unit between Al & Si.

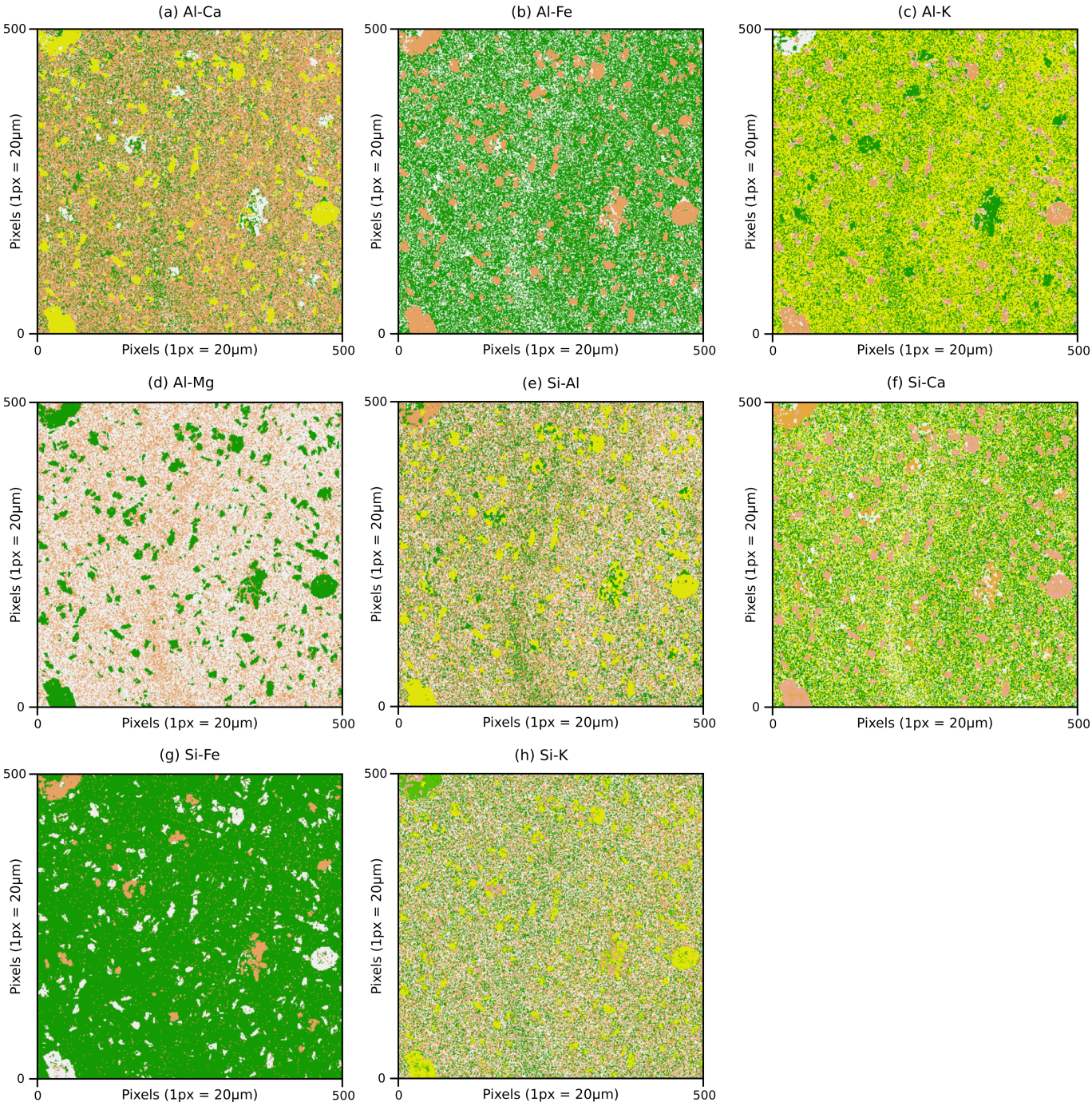

Fig. S2: Results of the individual finite mixture models for all combinations of elements in Table 2.

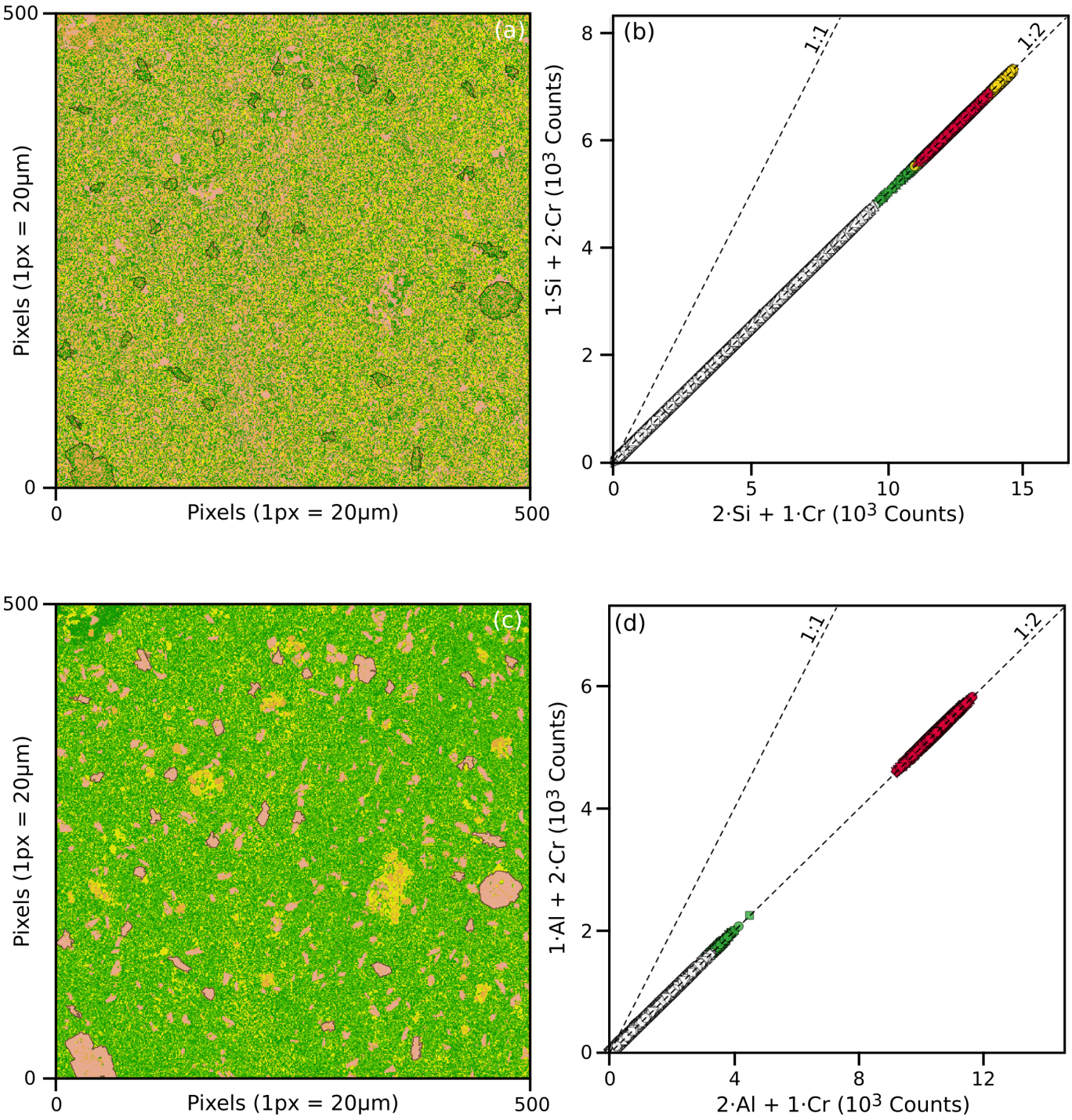

Fig. S3: Finite mixture model classification for (a-b) Si-Cr, and (c-d) Al-Cr. Segmented plagioclase are outlined in dark grey. Phases are only identified when there is significant variability in the network forming cation. Cr has no influence on the results of the finite mixture model.

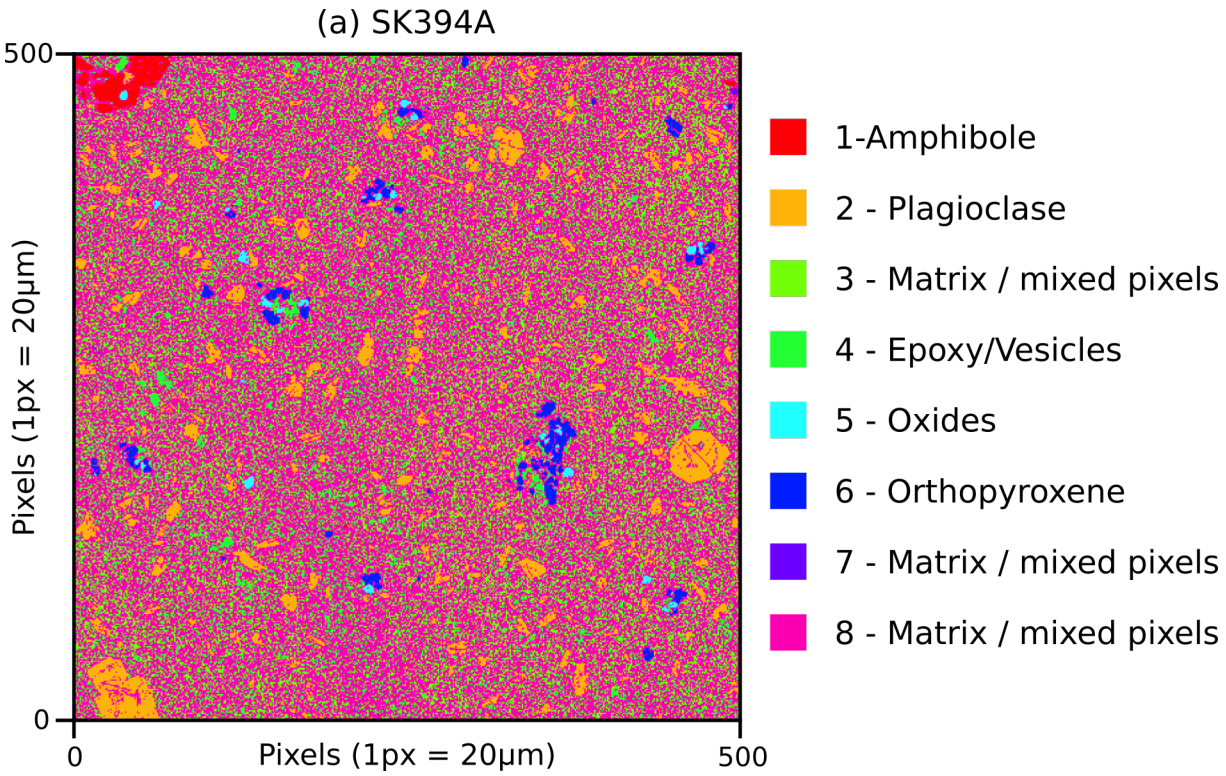

Fig. S4: The eight final discrete components that satisfy the *central pixel assumption* in SK394A.

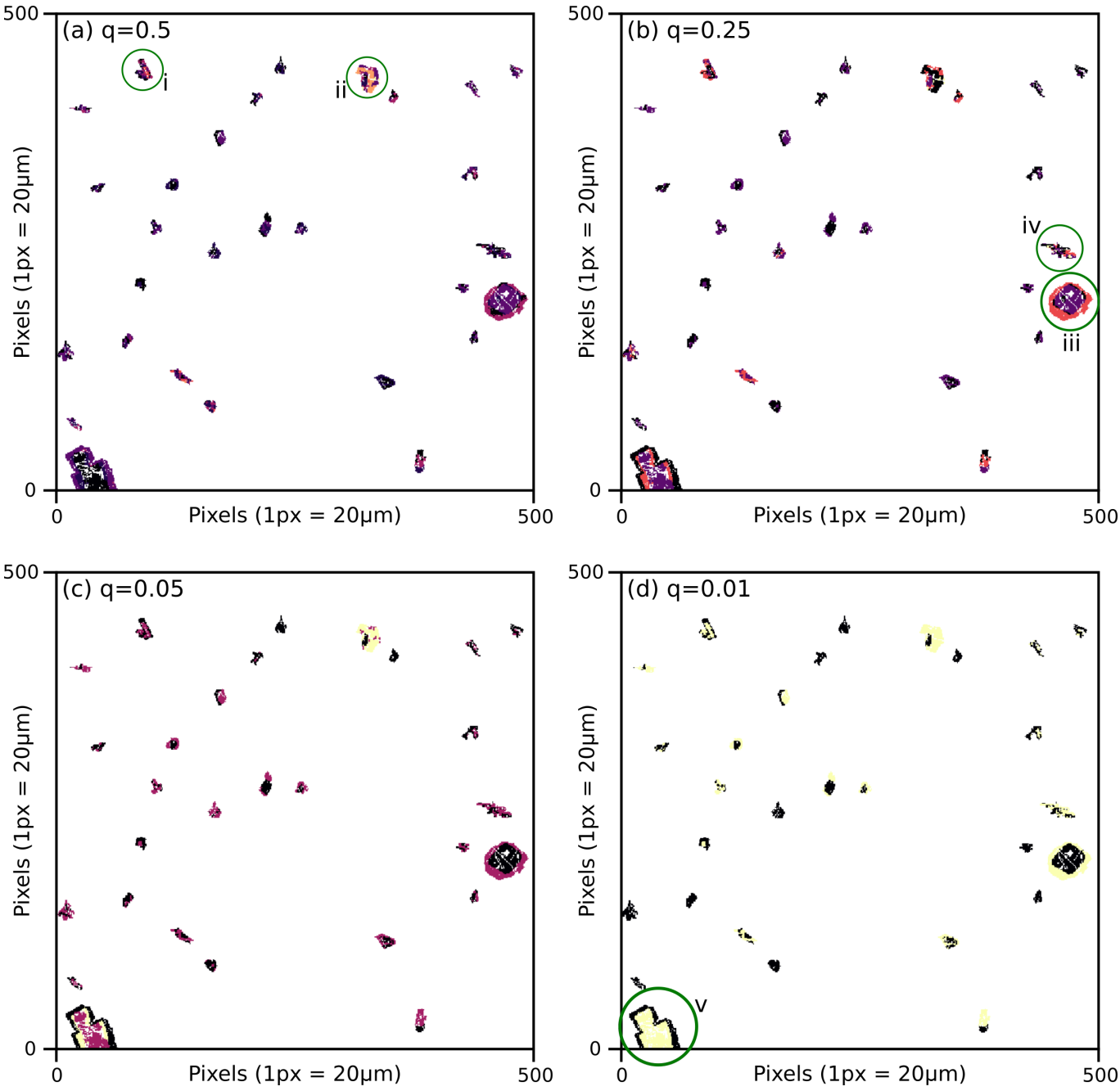

Fig. S5: Results of the affinity propagation for different percentile values (1/2th, 1/4th, 1/20th, 1/100th). You can see that for high percentile values the AP algorithm can segment the crystals into many zones, even over-fitting large crystals (e.g., i & ii). Higher percentile values can provide more information on crystal structure (e.g., iii – here the low Ca region in Figure 3 is identified), but may still over-segment noisy crystals (e.g., iv). Choosing too low values will reduce the number of potential zones, especially in larger crystals (e.g., v).

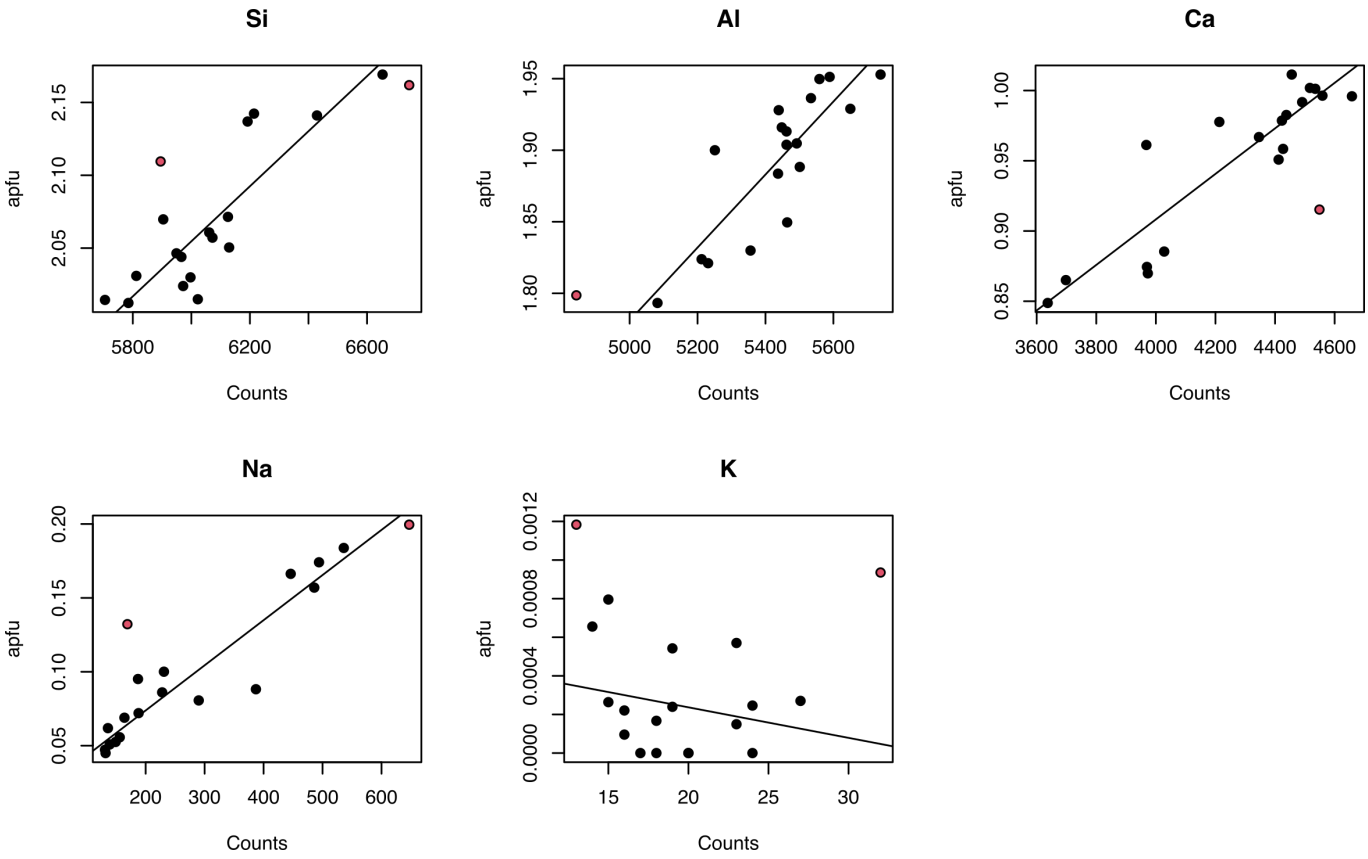

Fig. S6: Calibration of Si, Al, Ca, Na & K in plagioclase for the chemical maps. Outliers in red have been identified using the Cooks distance, and are not included in the calibration.

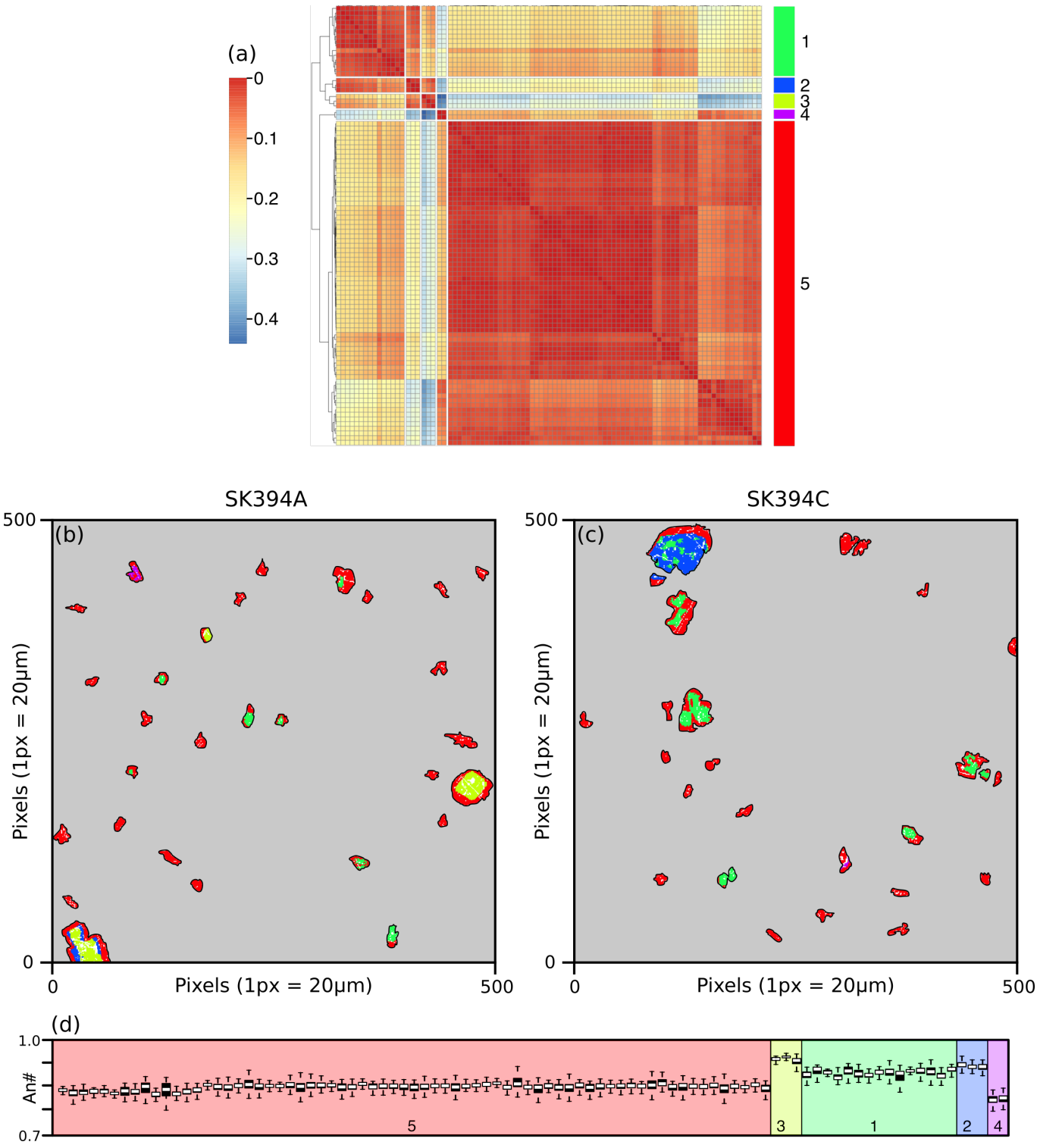

Fig. S7: Correlation of phenocryst zones when the results of the hierarchical clustering are split into five groups.

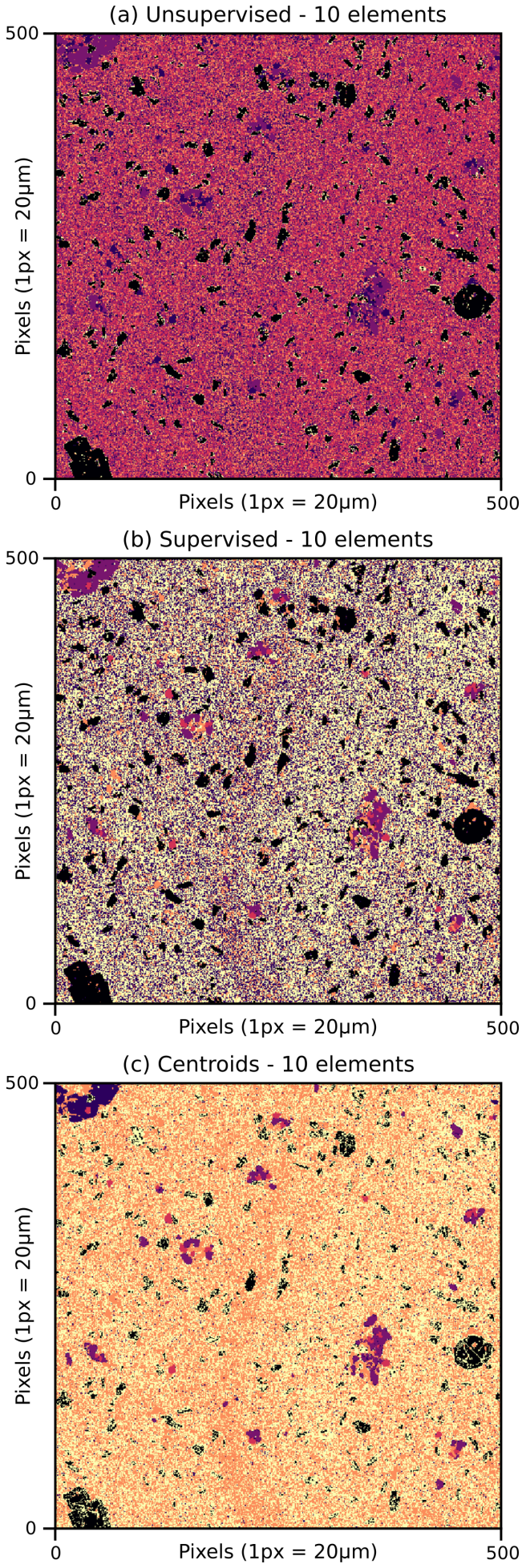

Fig. S8: Classification of 6 discrete components in SK394A using: (a) unsupervised k-means; (b) supervised k-means; and (c) a minimisation of the Euclidean distance to the mean value of each discrete component identified in Figure 1a. The mean values used in panel (c) are used to initiate the supervised approach in panel (b). All ten measured oxides have been used.

Table S1: 1. Results of the finite mixture models for SK394A & SK394C,
including whether the finite mixture model converged and if the results were included in the final classification of the thin section.

SK394A

	1	**2**	**3**	**4**	**5**	**6**	**7**	**8**	**9**
Elements1	Al	Al	Al	Al	Al	Si	Si	Si	Si
Elements2	Ca	Fe	K	Mg	Si	Ca	Fe	K	Mg
Converged	TRUE	TRUE	TRUE	TRUE	TRUE	TRUE	TRUE	TRUE	TRUE
Included	TRUE	TRUE	TRUE	TRUE	TRUE	TRUE	TRUE	TRUE	TRUE
Clusters	4	3	4	3	4	5	3	6	1

SK394C

	1	**2**	**3**	**4**	**5**	**6**	**7**	**8**	**9**
Elements1	Al	Al	Al	Al	Al	Si	Si	Si	Si
Elements2	Ca	Fe	K	Mg	Si	Ca	Fe	K	Mg
Converged	TRUE	TRUE	TRUE	TRUE	FALSE	TRUE	TRUE	TRUE	TRUE
Included	TRUE	TRUE	TRUE	TRUE	FALSE	TRUE	TRUE	TRUE	TRUE
max.Nk	4	3	4	4	5	5	2	4	2

Table S2: Composition of plagioclase point analyses in SK394A

Spot analyses - Oxides (wt. %)									
SiO2	Al2O3	Na2O	MgO	K2O	MnO	CaO	TiO2	FeO	Cr2O3
43.42	34.53	0.755	0.02	0.0045	0.0194	19.48	0.0186	0.4444	0
43.2	34.81	0.611	0.0426	0.0044	0	19.78	0.0058	0.5318	0
44.01	33.98	1.0429	0.0528	0.0041	0.0207	19.02	0.0297	0.5688	0
44.26	34.23	1.1026	0.0326	0	0.0079	18.96	0.024	0.4815	0.0119
46.3	32.68	2.03	0.0386	0.0157	0.014	17.29	0.0119	0.433	0
46.05	33.26	1.93	0.0331	0.0134	0	17.45	0	0.4745	0.0286
45.76	33.02	1.73	0.0223	0.0028	0.0152	17.66	0.0099	0.4959	0.0022
43.99	34.41	0.971	0.0287	0.0025	0.0049	19.15	0.0074	0.5221	0
43.09	35.44	0.5207	0.009	0.0037	0.0194	20	0	0.3545	0.018
42.96	35.34	0.4953	0.0144	0.0016	0.0237	20.15	0.0064	0.31	0
43.75	34.35	0.9439	0.0249	0	0.0177	19.19	0	0.4465	0
46.58	32.67	2.21	0.0382	0.0096	0.0042	17.01	0.0228	0.4778	0
45.85	33.31	1.84	0.0284	0.0199	0.0104	17.51	0.0225	0.4931	0
45.17	33.6	1.46	0.0367	0.011	0.0049	18.29	0.0129	0.5466	0
43.65	34.62	0.7922	0.0203	0	0	19.48	0.0056	0.5365	0
43.25	34.85	0.6795	0.0219	0.004	0.0042	19.71	0	0.5152	0
43.17	35.04	0.5776	0.0344	0	0.0092	19.93	0.0025	0.4158	0.013
43.23	35.49	0.5624	0.0277	0	0.0319	19.95	0.0028	0.5251	0
43.89	34.59	0.89	0.0218	0.0091	0.0362	19.53	0.0183	0.4986	0

Elemental maps (WDS) - Counts (Total)						Spot analyses - Ator				
Si	Al	Ca	Na	K		Si	Al	Na	Mg	K
5966	5448	4438	164	27		2.04396	1.91594	0.06891	0.00140	0.00027
5997	5439	4658	156	15		2.02993	1.92798	0.05567	0.00298	0.00026
5904	5437	4427	187	24		2.06974	1.88360	0.09510	0.00370	0.00025
6125	5501	4412	231	17		2.07145	1.88831	0.10006	0.00227	0.00000
6744	4843	3698	536	32		2.16186	1.79859	0.18379	0.00269	0.00094
6214	5212	3973	494	15		2.14232	1.82381	0.17410	0.00229	0.00080
6429	5231	4028	486	18		2.14106	1.82105	0.15695	0.00155	0.00017
6061	5251	3968	387	23		2.06072	1.89999	0.08820	0.00200	0.00015
5705	5739	4517	131	16		2.01444	1.95287	0.04720	0.00063	0.00022
5785	5589	4456	132	16		2.01235	1.95123	0.04499	0.00101	0.00010
6072	5462	4346	228	24		2.05719	1.90382	0.08606	0.00174	0.00000
6653	5082	3637	647	23		2.16914	1.79325	0.19955	0.00265	0.00057
6192	5356	3970	446	13		2.13691	1.82989	0.16628	0.00197	0.00118
5895	5464	4549	169	14		2.10949	1.84956	0.13221	0.00255	0.00066
5949	5462	4423	188	20		2.04644	1.91313	0.07202	0.00142	0.00000
5812	5650	4491	136	19		2.03094	1.92893	0.06187	0.00153	0.00024
5972	5534	4535	149	20		2.02399	1.93639	0.05251	0.00240	0.00000
6022	5559	4559	139	18		2.01490	1.94974	0.05083	0.00192	0.00000
6129	5492	4213	290	19		2.05046	1.90475	0.08062	0.00152	0.00054

ms per formula unit						
Mn	Ca	Ti	Fe	Cr		#An
0.00077	0.98258	0.00066	0.01750	0.00000		0.93
0.00000	0.99590	0.00020	0.02090	0.00000		0.95
0.00082	0.95845	0.00105	0.02237	0.00000		0.91
0.00031	0.95082	0.00084	0.01885	0.00044		0.90
0.00055	0.86504	0.00042	0.01691	0.00000		0.82
0.00000	0.86985	0.00000	0.01846	0.00105		0.83
0.00060	0.88537	0.00035	0.01940	0.00008		0.85
0.00019	0.96123	0.00026	0.02045	0.00000		0.92
0.00077	1.00185	0.00000	0.01386	0.00067		0.95
0.00094	1.01137	0.00023	0.01214	0.00000		0.96
0.00070	0.96686	0.00000	0.01756	0.00000		0.92
0.00017	0.84876	0.00080	0.01861	0.00000		0.81
0.00041	0.87443	0.00079	0.01922	0.00000		0.84
0.00019	0.91524	0.00045	0.02135	0.00000		0.87
0.00000	0.97858	0.00020	0.02104	0.00000		0.93
0.00017	0.99173	0.00000	0.02023	0.00000		0.94
0.00037	1.00122	0.00009	0.01630	0.00048		0.95
0.00126	0.99633	0.00010	0.02047	0.00000		0.95
0.00143	0.97765	0.00064	0.01948	0.00000		0.92